The project LIKE
Lidar Knowledge Europe
H2020-MSCA-ITN-2019, Grant no. 858358
is funded by the European Union




# D6.3 Determination of terrain-induced turbulence for air-safety considerations in the vicinity of airports by lidar measurements and LES simulations

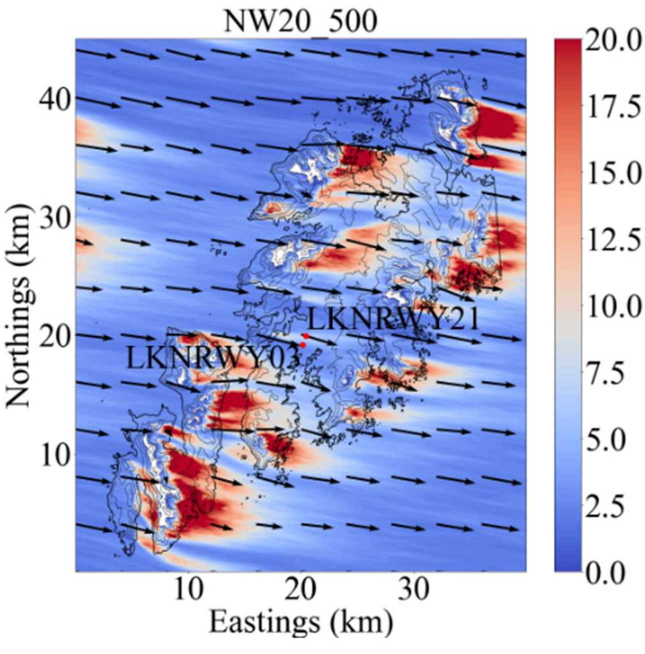



Authors: Joachim Reuder (UiB), Sai Wang (UiB), Ludovic Thobois (Vaisala/Leosphere), Frederik De Roo (Norwegian Meteorological Institute), Jose Laginha Palma (UoP), Isadora Coimbra (UoP), Olai Rune Hjetland (Avinor).


Publication: April 2023.
Duration: October 2019 to September 2023.
Co-ordinator: DTU Wind and Energy Systems.

Report: D6.3 Determination of terrain-induced turbulence for air-safety considerations in the vicinity of airports by lidar measurements and LES simulations



Front page: Left: lidar deployed on the Lofoten islands (photo: Avinor); Right: Results of LES simulations for the vicinity of Leknes airport (from Wang et al., 2022)

Publisher: University of Bergen, 5020, Bergen, Norway; DOI: 10.5281/zenodo.7839966

# Preface

The 15 Early Stage Researchers (ESRs) in the LIKE project investigate topics in which lidar plays a significant role. This report summarises the potential and applications of lidars for estimating and investigating terrain-induced turbulence since it is an important parameter in the design and planning of airports in complex terrain. The Large Eddy Simulation modelling is presented here as a novel tool for systematically investigating terrain-induced turbulence hazards. Also, a short description is given for two available lidar data sets measured near two exposed airports: the Leknes airport on Lofoten Island in Northern Norway and the Funchal airport on Madeira Island, Portugal.

# Contents

# Executive summary

This report will explore the modelling and measurement of turbulence as an aviation wind hazard, focusing on the importance of lidar technology to the subject. Turbulence is an essential parameter for airport activities, as it impacts the safety of passengers and aircraft, the planning of new airports, and airline costs. The modelling will cover a case study at Lofoten Island, where an LES model is employed to assess terrain-induced turbulence. The measurements will explore Doppler lidar data acquired at two sites: Lofoten and Madeira Islands. The measurement studies are in their initial stages and will be part of ESR15 and ESR5 future works.

# 1. Introduction

Atmospheric turbulence is a potential aviation hazard in basically any flight stage (Sharman and Lane, 2016; Gultepe et al., 2019). It refers to rapid, irregular changes in the wind speed and direction that can occur in the atmosphere and impose a major concern to aviation, not only for passengers' comfort but also for safe and efficient aircraft operations. As summarised by the World Meteorological Organization (WMO) (WMO, 2022) the main turbulent hazards are described as follows: (1) clear-air turbulence (CAT) is usually encountered at the cruise altitude levels in the upper troposphere or lower stratosphere; (2) boundary layer turbulence (BLT) typically occurring in the lowest one or two kilometres, thus affecting the take-off and landing approach; and (3) low-level turbulence (LLT), which happens very close to the ground and is thus important for the final approach and touch-down.

The two main mechanisms for the creation of turbulence in the atmosphere are wind shear and buoyancy (e.g., Stull, 1988), with their relative importance differing among the categories introduced above. CAT can be triggered by Kelvin-Helmholtz instabilities (Sharman et al., 2012; Trier et al., 2012) created by wind shear, the amplification, overturning and breaking of mountain waves (Kim and Chun, 2011; Doyle et al., 2011), or in the vicinity of large convective clouds (Lane et al., 2012). Thermal updrafts can induce BLT in daytime convective boundary layers, as well as strong wind shear, and mechanical forcing associated with complex terrain. LLT is usually caused by wind shear and obstacles on the ground, e.g., the local topography close to the airport (Belo-Pereira and Santos, 2020), buildings and higher surface vegetation (Hon et al., 2020), or turbulence induced by starting and landing aircraft (Basse, 2020; Lunnon, 2016). Prominent examples of airports that are adversely affected by turbulence conditions are Hong-Kong (Chan, 2011), Madeira (Belo-Pereira and Santos, 2020), Innsbruck in the Austrian Alps, and some smaller and larger airports in Norway, as Alta (Rasheed and Mushtag, 2014) or Trondheim Værnes.

This report will focus on terrain-induced BLT in the vicinity of airports, which particularly endangers the glide path during the approach for landing. During landing, the aircraft is relatively slow and operates with reduced engine power, reducing manoeuvrability and corresponding limited reaction capability to external turbulent disturbances. Features of low-level wind shear and turbulence are known to follow spatial and time scales on the order of a few hundred meters and tens of seconds, making ground-based remote sensing measurements of high spatiotemporal resolution the primary choice for their observation and detection. Thus, we will address terrain-induced BLT under the aspect of air safety by a novel approach combining high-resolution numerical modelling with observations from long-range Doppler wind lidar systems.

So far, lidar measurements related to air safety have mainly been limited to LLT. Hong Kong Observatory (HKO) (Chan, 2009, 2011, 2016; Hon and Chan, 2020) was the first meteorology office in the world to develop and implement a low-level turbulence alert system. Due to the complex orography in its vicinity, Hong Kong Airport is frequently affected by low-level wind shear and turbulence. Doppler lidars were used to generate automatic wind shear and turbulence alerts to mitigate those wind hazards to air traffic. The turbulence alerts are based on the eddy dissipation rate (EDR), calculated by the structure function of the flow, derived from the difference of Doppler velocities measured at two points, spaced of a certain distance with high-resolution azimuthal scans. The algorithm was based on the work of Frehlich, 2001, and EDR is the chosen metric to characterise atmospheric turbulence for aviation by the International Civil Aviation Organization (ICAO). Compared to flight data, retrieved EDR data with a Doppler lidar had a mean error of 20%. These values were used successfully to issue turbulence alerts with a probability of detection of 80%. Maps of EDR were also provided to support the forecasters at the airport. They revealed that the tall Congress building just a few hundred meters upstream of the runway induced a significant part of the turbulence that affected one of the runways.

One attempt to address BLT for air safety was undertaken at Keflavik Airport in Iceland (Yang et al., 2020) by studying vertical profiles of EDR based on the algorithm developed by Frehlich, 2001. The EDR profiles allowed them to determine at which altitude the turbulence occurred as well as its horizontal position relative to the lidar.

# 2. LES modelling of terrain-induced turbulence

A turbulence modelling case study is going to be explored in this report, where PALM (Maronga et al., 2015) Large-Eddy Simulations (LES) model is employed at the Lofoten Island (Norway). The main results are summarized here, and a published paper (Wang et al., 2022) with extended results is attached to this report.

## 2.1 Lofoten island

As a first step, we performed a series of systematic LES model runs for the 16 cardinal wind directions and two different geostrophic wind speeds of 10 m/s and 20 m/s. This study (Wang et al., 2022; attached in this report) investigates the turbulence conditions in the surroundings of the existing Leknes airport (LKN) in the Lofoten islands. We studied the terrain-induced turbulence in the atmospheric boundary layer and performed a turbulence risk analysis on an idealised aircraft trajectory for different geostrophic wind speeds and directions. To achieve these goals, a suite of simulation runs was carried out using the LES model PALM, based on a high-resolution topography dataset near the LKN airport in the Lofoten islands. Based on initial parametric sensitivity studies, we have chosen a grid spacing of 50 m and a simulation time of 12 h for a suite of model simulations for 16 different wind directions and two geostrophic wind speeds (10 m/s and 20 m/s). The results show that PALM can properly simulate turbulent flows for air safety-related investigations in an extended domain with high resolution and at an acceptable computational expense.

According to the simulation results of the wind field and turbulence in the whole domain, we demonstrated that the topographically-induced turbulence occurs in the lee of steep mountains and ridges. These terrain-induced turbulence patterns typically extend 5 to 10 km downstream, indicating of a slight increase in this extension with altitude. The highest turbulent kinetic energy (TKE) levels are observed in the middle of the atmospheric boundary layer (ABL), around 500 m altitude, more or less corresponding to the level of turbulence induced by terrain features in the free flow.

A turbulence risk analysis along idealised flight trajectories shows that the turbulence risk conditions are substantially determined by the wind conditions and their interaction with the topography. Concerning wind speed, the results indicate that for a geostrophic flow below 10 m/s, the risk of aviation critical terrain-induced BLT is rather low in the vicinity of LKN. At 20 m/s the situation has completely changed; the aviation critical threshold of 9 $m^2/s^2$ is exceeded for 14 out of 16 investigated wind directions. Two main factors influence the observed directional dependency of the turbulence risk, the topography’s orientation with respect to the wind direction and the fetch, i.e., the average upstream surface characteristics. Turbulent eddies in the lee form are particularly efficient when the flow intersects almost perpendicularly with the steep topography. The orographical form drag also plays an important role, as it affects the average wind speed of the upstream flow. The main topographic features are SW to NE oriented, with an average altitude decreasing from NW to SE. However, the southwestern mountains, mainly on Flakstadøya, run north to south. From the profiles and statistics observed, for the southwestern glide slope RWY02, the highest turbulence risk occurs under westerly winds, and for the northeastern glide slope RWY20, the highest turbulence risk is associated with northwesterly winds.

This study presents a novel methodology as it uses, for the first time, a systematic LES modelling approach to investigate the turbulence characteristics for two geostrophic wind speeds and 16 different wind directions. Although the simulations already cover a considerable range of relevant meteorological conditions for the operation of a future airport, this study still comprises a limited subset of cases, particularly for higher wind speeds from critical wind directions. This is, however, beyond the scope of this proof-of-concept study. It should also be emphasised that this study's choice of aircraft trajectories is rather idealistic. Nevertheless, it already provides a very good indication of the aviation-relevant BLT risks in the vicinity of LKN. The design of our method allows, in addition, for an easy adaptation as soon as more detailed flight route information for take-off and landing will be available in the future.

# 3. Lidar measurements of terrain-induced turbulence

Another option to collect information on air-traffic-related turbulence risks, besides computational modelling, is utilising on-site measurements. Therefore, this section explores ground-based measurements at two sites of interest: Lofoten and Madeira Islands.

## 3.1 Lofoten island

Between October 2018 and April 2019, Kjeller Vindteknikk (Norconsult) conducted on behalf of Avinor a lidar measurement campaign at several potential locations for a new/extended airport for the Lofoten islands. The locations and the main runway parallel scan direction are shown in Figure 1. The corresponding experiment periods are summarised in Table 1.

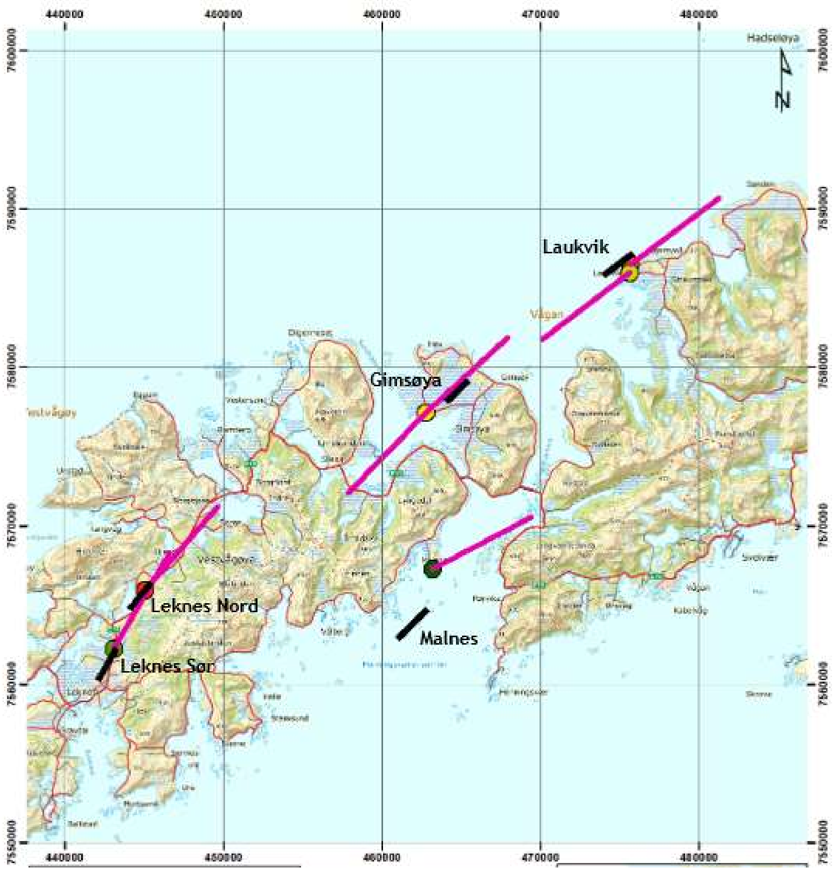


**Figure 1:** Location of the lidar measurements during the Avinor campaign on the Lofoten islands. The purple lines indicate the scanning direction of the lidar beam, and the black ones the direction of the corresponding runways. Adapted from KVT, 2019.

The instruments used were 4 Doppler wind lidar systems (Leosphere WindCube WLS400) that mainly operated in runway-parallel stirring mode at an elevation angle of 3 deg, resembling the idealised glide path of an aircraft during the final approach for landing. This measuring mode provides high-resolution time series (ca. 1 Hz) of the line-of-sight (LOS) velocity along the lidar beam. Avinor has lately provided the data for scientific use in the LIKE project, and a basic quality control and analysis of the raw data has started as part of the research performed by ESR15. The average data availability at a distance of one nautical mile was slightly above 90%, reducing to about 66% for two nautical miles (KVT, 2019).

**Table 1:** Location and period of the lidar measurements during the Avinor campaign on the Lofoten islands. Adapted from KVT, 2019.

| Lidar position | Scan direction | Start date | End date | Number of days |
|---|---|---|---|---|
| Laukvik | NE | 10.10.2018 | 10.01.2019 | 93 |
| Laukvik | SW | 08.03.2019 | 10.04.2019 | 33 |
| Gimsøy | NE | 10.10.2018 | 16.01.2019 | 99 |
| Gimsøy | SW | 16.01.2019 | 10.04.2019 | 83 |
| Malnes | NE | 10.10.2018 | 16.01.2019 | 99 |
| Leknes North | NE | 23.01.2018 | 10.04.2019 | 76 |
| Leknes South | NE | 10.10.2018 | 10.04.2019 | 182 |

Figure 2 shows the hourly averaged LOS velocity measured at Leknes South for about half a year, between 10.10.2018 and 10.04.2019. The y-axis indicates the distance of the measurement point from the lidar. The maximum distance plotted (7000 m) corresponds to the chosen elevation angle (3 deg) to an elevation of 366 m above the lidar position. Red colours indicate positive values of the LOS velocity, i.e., a South-Westerly wind component resulting in flow away from the lidar.

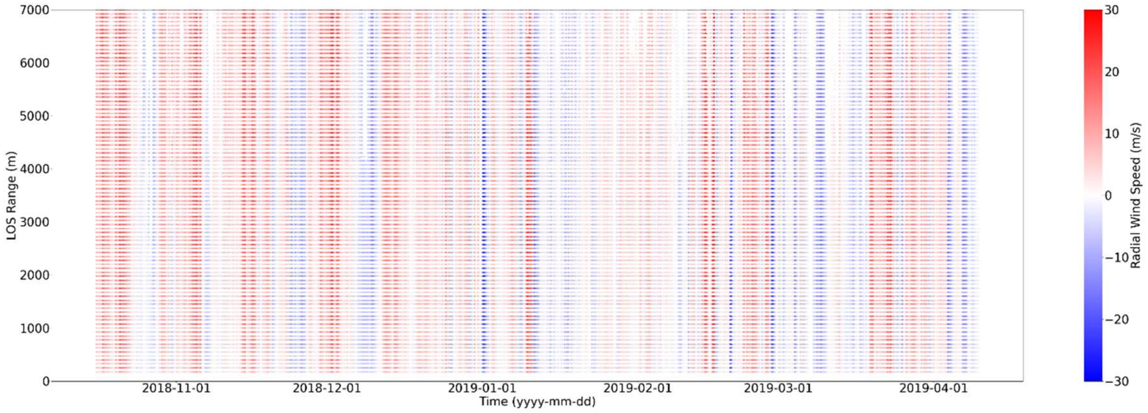


**Figure 2**: Hourly averages of LOS velocity measured at Leknes South from 10.10.2018 to 10.04.2019 as a function of the distance from the lidar. Red colours indicate that the flow moves away from the lidar, while blue indicates the movement towards the lidar.

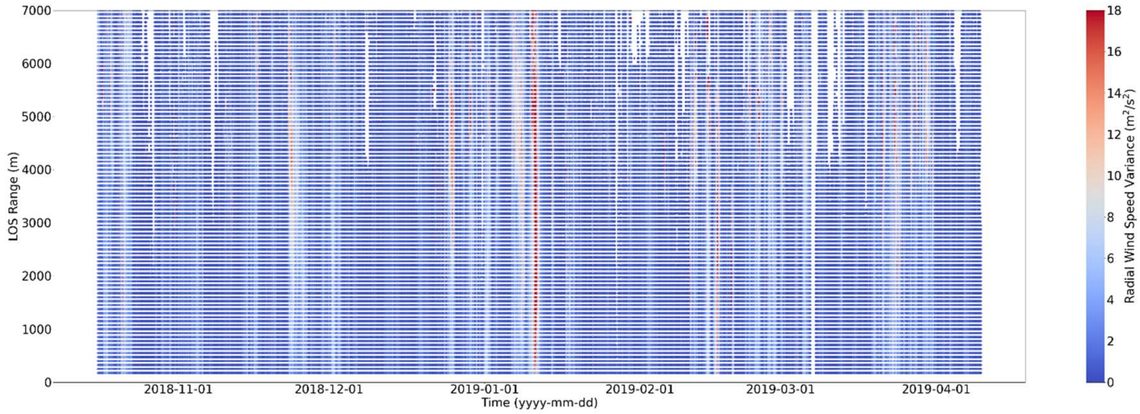


**Figure 3**: Standard deviation of LOS velocity over a 1-hour period, measured at Leknes South from 10.10.2018 to 10.04.2019, as a function of the distance from the lidar. Reddish colours indicate values exceeding the threshold for potentially hazardous flight conditions.

Figure 3 shows the corresponding standard deviation of the LOS velocity over one hour. Reddish colours indicate values exceeding the threshold of 9 $m^2/s^2$, indicating potentially hazardous flight conditions (Wang et al., 2022). Based on that plot, we have identified 5 high-risk events that will be analysed in more detail, forming the basis of an extensive comparison with LES modelling results for the next manuscript of ESR15.

# 3.2 Madeira

Located in the subtropical region (32.7°N, 16.9°W), Madeira Island, the largest island of the Madeira Archipelago, with 22 km width and 57 km length, has tourism as one of its main economic sources. The most common way to arrive at the island is by its airport. The Madeira International Airport (MIA), also known as Cristiano Ronaldo International Airport, is placed in the SE region of the island, near the shore, at Santa Cruz City.

The island has a volcanic origin and presents a complex terrain, with a mountain range oriented in the WNW-ESE direction. Just close to the airport, critical geographic formations modify and induce local flows in the vicinity and at the airport (Figure 4). To the right side of the runway, there is mainly the Atlantic Ocean; to the left, a steep mountain; and just after the runway threshold, there are valleys. Near the RNW23 is the Machico Valley, while just after the RNW05 is Santa Cruz Valley.

MIA is considered by many as a challenging airport to operate since in the island there is the occurrence of strong wind shear (Miranda et al., 2020), island-induced wakes (Grubisic et al., 2015; Caldeira et al., 2014), turbulence (Belo-Pereira and Santos, 2020), hydraulic jumps (Grubisic et al., 2015), internal atmospheric waves (Araujo et al., 2010), and tip jets (Miranda et al., 2020). Adverse weather conditions restrict the landing/departure of aircrafts on the island (Belo-Pereira and Santos, 2020), causing an economic loss for airlines, which end up using more fuel to divert the route or wait for more favourable weather conditions, and for the island itself, which receives fewer tourists when flights are diverted.

Aiming to assess the weather conditions that most influence the Madeira airport operations, a lidar was installed in MIA in 2021, by the Instituto Português do Mar e da Atmosfera (IPMA), and it is in operation until nowadays. The equipment is located almost in the middle of the runway, on its west side, on top of a small building, which houses a pump system (Figure 5). The equipment is a 100s unit from Leosphere and was configured with Plan Position Indicator (PPI), Range Height Indicator (RHI), and Doppler Beam Swinging (DBS) scans. The PPI scan has an elevation angle equal to 3°, swapping the runway from 42° to 220° azimuth. The RHI was configured with an azimuth angle of 42° and elevation angles from 0° to 180°. Instantaneous snapshots of PPI and RHI measurements are depicted in Figure 6.

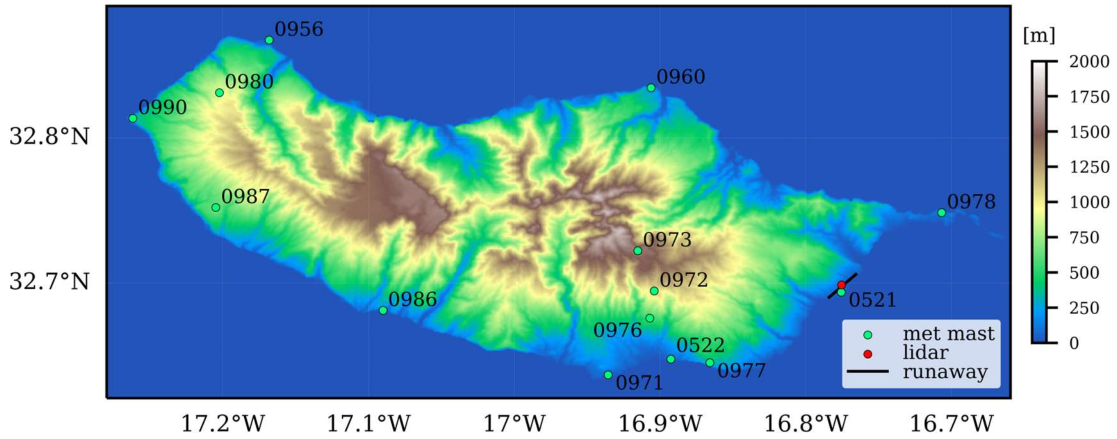


**Figure 4**: Madeira Island terrain representation from SRTM depicting the location of meteorological masts, a Doppler lidar, and the airport runway.

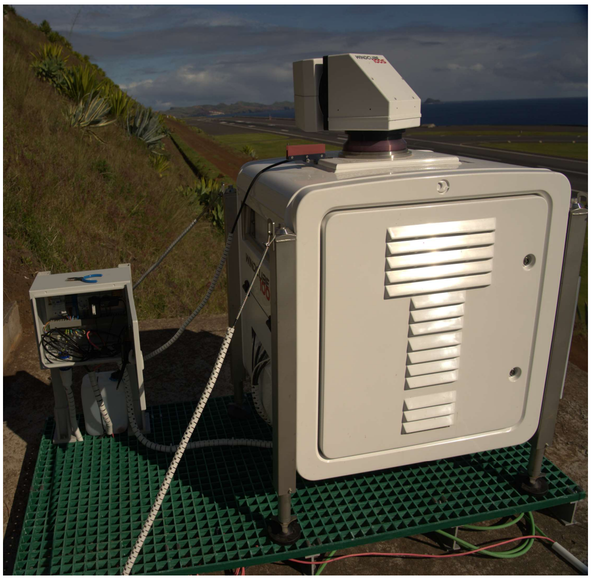

**Figure 5**: The 100s lidar unit installed at the Madeira island airport.

The analysis of the lidar data is in its initial stages and will be part of the work developed by the ESR5 of the LIKE project. The goal is to perform a study employing lidar and meteorological measurements since the island also has a network of automatic meteorological stations (AME), Figure 4, together with meso-to-microscale simulations. The simulations, with the Weather Research and Forecasting (WRF) (Skamarock et al., 2019) and VENTOS®/M (Rodrigues et al., 2015) unsteady Reynolds-Averaged Navier-Stokes (uRANS) models, enable a broader view of the flow beyond the measurement spatial and temporal resolutions. In contrast, the measurements allow the validation of the simulations at the same resolutions.

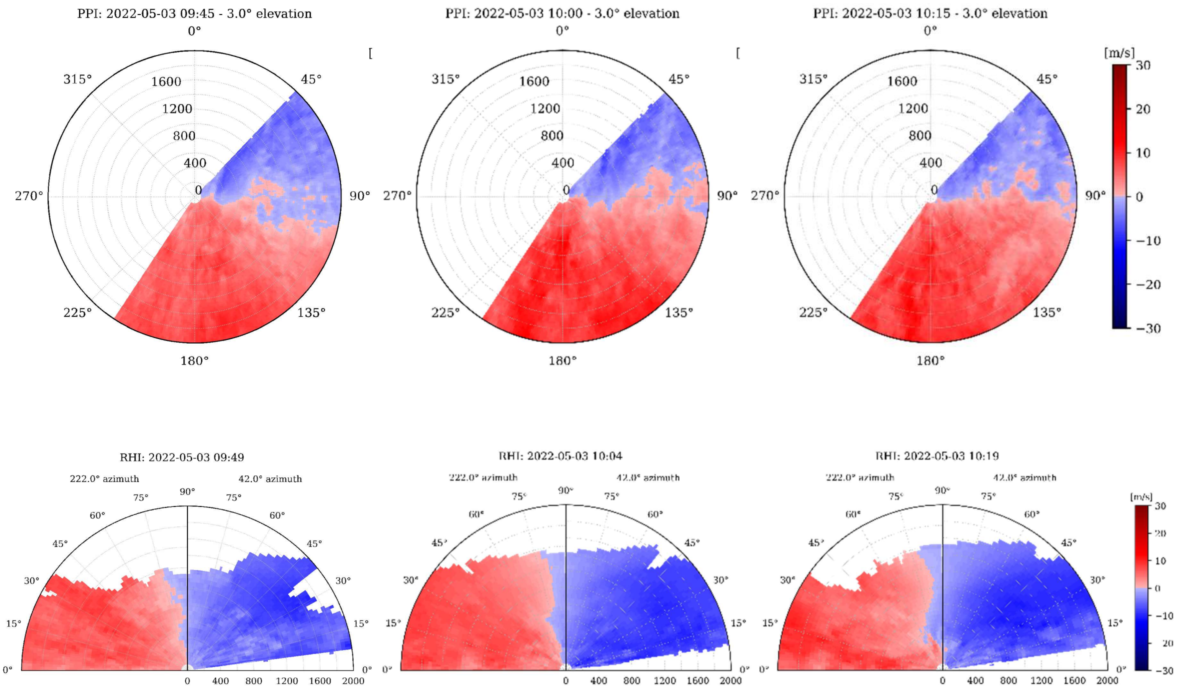


**Figure 6**: PPI (upper) and RHI (lower) instantaneous scans at the Madeira airport. The positive LOS velocities (red colours) represent the wind flowing away from the lidar, while the negative LOS values (blue colours) represent the flow moving towards the lidar.

# 4. Conclusion

This report aimed to give a perspective on using Doppler lidar and high-resolution computational modelling for turbulence assessment of the wind flow in the vicinity and at airports. Turbulence studies can add to the siting of new airports, improve the safety of airport activities (mainly during take-off and landing) and their efficiency, and reduce airline costs, for example.

The Lofoten Islands study, which explored PALM LES simulations of terrain-induced turbulence at the Leknes airport, showed that high-resolution turbulence modelling is a valuable tool in characterising this phenomenon. The results enabled the identification of the turbulence extension and its unwanted effects on the islands. The turbulence was observed between 5 and 10 km after the ridges, on the leeward side of steep mountains. Additionally, an idealized flight trajectory analysis characterized the adverse turbulence features according to wind conditions (wind speed and direction). For RNWY03, westerly winds depicted a higher occurrence of turbulence risks, while for RNW32, northwest winds showed a higher association with turbulence risks.

The studies of Lofoten and Madeira islands measurements with Doppler lidars are in their initial stages, but future analyses will be developed by ESRs 15 and 5. With the advance of the Doppler lidar technology and its understanding, it is expected that the lidar measurements at these two locations enable a deeper comprehension of the flow and adverse atmospheric conditions to the airport activities, such as turbulence.

# References

Araujo, I.B.; Caldeira, R.; Couvelard, X. Island induced (sub) mesoscale features around Madeira archipelago (initial findings). In Proceedings of the 3rd International workshop SeaSAR, 2010.

Basse, N. T. (2020). Modelling of vortex-induced aviation turbulence. Meteorol. Atmos. Phys., 2020, 132(3), 401–411. doi:10.1007/s00703-019-00699-0.

Belo-Pereira, M., & Santos, J. A. Air-traffic restrictions at the Madeira International Airport due to adverse inds: links to synoptic-scale patterns and orographic effects. Atmosphere, 2020, 11(11), 1257. doi:10.3390/atmos11111257.

Caldeira, R. M. A.; Stegner, A.; Couvelard, X.; Araújo, I. B.; Testor, P.; Lorenzo, A. Evolution of an oceanic anticyclone in the lee of Madeira Island: In situ and remote sensing survey. J. Geophys. Res. Oceans, 2014, 119, 1195– 1216, doi:10.1002/2013JC009493.

Chan, P. W. LIDAR-based turbulence intensity for aviation applications. In Aviation Turbulence (pp. 193–209), 2016. Cham: Springer International Publishing. doi:10.1007/978-3-319-23630-8_9.

Chan, P. W., Atmospheric turbulence in complex terrain: Verifying numerical model results with observations by remote-sensing instruments. Meteorology and Atmospheric Physics, 2009, 103(1–4), 145–157. doi:10.1007/s00703-008-0342-3.

Chan, P. W. Generation of an eddy dissipation rate map at the Hong Kong International Airport based on Doppler lidar data. Journal of Atmospheric and Oceanic Technology, 2011, 28(1), 37–49. doi:10.1175/2010JTECHA1458.1.

Doyle, J.D.; Jiang, Q.; Smith, R.B.; Grubiši´c, V. Three-dimensional characteristics of stratospheric mountain waves during T-REX. Mon. Weather Rev. 2011, 139, 3–23. doi:10.1175/2010MWR3466.1.

Frehlich, R. Estimation of velocity error for Doppler lidar measurements. J. Atmos. Oceanic Technol. 2001, 18, 1628–1639. doi:10.1175/1520-0426(2001)018<1628:EOVEFD>2.0.CO;2.

Grubišić, V., Sachsperger, J.; Caldeira, R. Atmospheric Wake of Madeira: First Aerial Observations and Numerical Simulations. Journal of the Atmospheric Sciences, 2015, 72(12) pp. 4755-4776. doi: 10.1175/JAS-D-14-0251.1.

Gultepe, I.; Sharman, R.; Williams, P.D.; Zhou, B.; Ellrod, G.; Minnis, P.; Trier, S.; Griffin, S.; Yum, S.S.; Gharabaghi, B.; et al. A Review of high impact weather for aviation meteorology. Pure Appl. Geophys. 2019, 176, 1869–1921. doi:10.1007/s00024-019-02168-6.

Hon, K.K.; Chan, P.W. Alerting of hectometric turbulence features at Hong Kong International Airport using a short-range LIDAR. Meteorol. Appl. 2020, 27, 1–10. doi:10.1002/met.1945.

Kim, J.H.; Chun, H.Y. Statistics and possible sources of aviation turbulence over South Korea. J. Appl. Meteorol. Climatol. 2011, 50, 311–324. doi:10.1175/2010JAMC2492.1.

KVT, Lofoten - Værmessig tilgjengelighet for aktuelle flyplasslokaliteter, Kjeller Vindteknik, 2019, Report KVT/HÁ/2019/R049 Rev1.

Lunnon, B. Turbulence events interpreted by vortex rolls. In Aviation Turbulence, 2016, pp. 83–94. Cham: Springer International Publishing. doi:10.1007/978-3-319-23630-8_4.

Maronga, B.; Gryschka, M.; Heinze, R.; Hoffmann, F.; Kanani-Sühring, F.; Keck, M.; Ketelsen, K.; Letzel, M. O.; Sühring, M.; Raasch, S. The Parallelized Large-Eddy Simulation Model (PALM) version 4.0 for atmospheric and oceanic flows: model formulation, recent developments, and future perspectives. Geosci. Model Dev., 2015, 8, 1539-1637. doi:10.5194/gmd-8-2515-2015.

Miranda, P. M. A.; Tomé, R.; Frois, L.; Nogueira, M.; Alves, J.M.R.; Prior, V.; Caldeira, R.; Dutra, E. Speed-up of the Madeira tip jets in the ERA5 climate highlights the decadal variability of the Atlantic subtropics. Q J R Meteorol Soc. 2021; 147: 679– 690. doi:10.1002/qj.3940.

Rasheed, A., & Mushtaq, A. Numerical analysis of flight conditions at the Alta airport, Norway. Aviation, 2014, 18(3), 109–119. doi:10.3846/16487788.2014.969885.

Rodrigues, C.V.; Palma, J.M.L.M.; Rodrigues, Á.H. Atmospheric flow over a mountainous region by a one-way coupled approach based on Reynolds-Averaged turbulence modelling. Boundary-Layer Meteorol, 2016, 159, 407–437. doi: 10.1007/s10546-015-0116-7.

Sharman, R.; Lane, T. (Eds.), Aviation Turbulence; Springer International Publishing: Cham, Switzerland, 2016. doi:10.1007/978-3-319-23630-8.

Sharman, R.D.; Trier, S.B.; Lane, T.P.; Doyle, J.D. Sources and dynamics of turbulence in the upper troposphere and lower stratosphere: A review. Geophys. Res. Lett. 2012, 39. doi:10.1029/2012GL051996.

Skamarock, W. C.; Klemp, J. B.; Dudhia, J.; Gill, D. O.; Liu, Z.; Berner, J.; Wang, W.; Powers, J. G.; Duda, M. G.; Barker, D. M.; Huang, X.-Y. A description of the Advanced Research WRF version 4. NCAR Tech. Note NCAR/TN-556+STR, 2019, 145 pp. doi:10.5065/1dfh-6p97.

Stull, R.B. An Introduction to Boundary Layer Meteorology; Springer: Dordrecht, The Netherlands, 1988. doi:10.1007/978-94-009-3027-8.

Trier, S.B.; Sharman, R.D.; Lane, T.P. Influences of Moist Convection on a Cold-Season Outbreak of Clear-Air Turbulence (CAT). Mon. Weather Rev. 2012, 140, 2477–2496. doi:10.1175/MWR-D-11-00353.1.

Lane, T.P.; Sharman, R.D.; Trier, S.B.; Fovell, R.G.; Williams, J.K. Recent Advances in the Understanding of Near-Cloud Turbulence. Bull. Am. Meteorol. Soc. 2012, 93, 499–515. doi:10.1175/BAMS-D-11-00062.1.

WMO. Aviation|Hazards|Turbulence and Wind Shear. Available online: https://community.wmo.int/activity-areas/aviation/hazards/turbulence (accessed on 1 March 2022)

Yang, S.; Petersen, G.N.; von Löwis, S.; Preißler, J.; Finger, D.C. Determination of eddy dissipation rate by Doppler lidar in Reykjavik, Iceland. *Meteorol Appl*. 2020; 27:e1951. doi:10.1002/met.1951.

# Appendix

*atmosphere*

*Article*

# Characterization of Terrain-Induced Turbulence by Large-Eddy Simulation for Air Safety Considerations in Airport Siting

**Sai Wang [1,*], Frederik De Roo [2], Ludovic Thobois [3] and Joachim Reuder [1]**

1 Geophysical Institute, Bergen Offshore Wind Centre (BOW), Bjerknes Centre for Climate Research, University of Bergen, Allégaten 70, 5007 Bergen, Norway; joachim.reuder@uib.no
2 The Norwegian Meteorological Institute, 0313 Oslo, Norway; frederikdr@met.no
3 Vaisala France, 6A Rue René Razel, 91400 Saclay, France; ludovic.thobois@vaisala.com
* Correspondence: sai.wang@uib.no

**Abstract:** Topography-induced turbulence poses a potential hazard for aviation safety, in particular during the final approach and landing. In this context, it is essential to assure that the impact of topography-induced turbulence on the flight paths during take-off and landing is minimized already during the design and planning phase. As an example of the siting and planning of a potential new airport in complex terrain, this study investigates the distribution of terrain-induced boundary layer turbulence in the vicinity of the current Lofoten airport at Leknes (LKN). For that purpose, large-eddy simulations (LES) have been performed with the PAralellized Large-eddy Simulation Model (PALM) on a $40 \times 45 \times 4$ km$^3$ computational domain around LKN. An initial parametric sensitivity study resulted in a grid spacing of 50 m and an overall simulation time of 12 h for our individual model runs. A suite of 32 model simulations for 16 different wind directions and two geostrophic wind speeds of 10 ms$^{-1}$ and 20 ms$^{-1}$, was then performed and analysed. A turbulence risk analysis along idealized flight trajectories shows that the high-risk conditions are substantially determined by the wind conditions and their interaction with the topography. With respect to wind speed, the results indicate that for a geostrophic flow below 10 ms$^{-1}$, the risk of aviation critical, terrain-induced boundary layer turbulence (BLT), is rather low in the vicinity of LKN. At 20 ms$^{-1}$ the situation has completely changed, as for 14 out of 16 investigated wind directions the 9 m$^2$s$^{-2}$ aviation critical threshold of turbulent kinetic energy per unit air mass (*TKE*) is exceeded. In the northwesterly wind scenarios, the largest areas with critical turbulence in the vicinity of LKN are observed.

**Keywords:** atmospheric boundary layer; terrain-induced turbulence; large-eddy simulation; aviation safety; airport siting

**Citation:** Wang, S.; De Roo, F.; Thobois, L.; Reuder, J. Characterization of Terrain-Induced Turbulence by Large-Eddy Simulation for Air Safety Considerations in Airport Siting. *Atmosphere* **2022**, *13*, 952. https://doi.org/10.3390/atmos13060952

Academic Editors: Pak-Wai Chan and Jung-Hoon Kim

Received: 18 April 2022
Accepted: 2 June 2022
Published: 11 June 2022



## 1. Introduction

Turbulence refers to rapid, irregular changes in the wind speed and direction that are present in the atmosphere and is a major concern to aviation, not only for passengers' comfort, but also for safe and efficient aircraft operations [1,2]. Encountered by the aircraft, turbulence brings sudden jumps and jolts that can compromise safety, in particular during the landing approach, when the aircraft is relatively slow and its manoeuvrability correspondingly low. In severe cases, abrupt changes in altitude of the aircraft may occur and the pilot may suffer a momentary loss of control. As a consequence, pilots, dispatchers and aircraft controllers attempt to avoid turbulence whenever possible.

In general, turbulence can appear in different forms and at any stage during a flight, as, summarized by the World Meteorological Organization (WMO) [3]: clear-air turbulence (CAT) is usually encountered at the cruise altitude levels in the upper troposphere; boundary layer turbulence (BLT), typically occurring in the lowest one or two kilometres, thus affecting the take-off and landing approach; and low-level turbulence (LLT), which happens very close to the ground, and thus important for the final approach close to touch-down.

The two main mechanisms for the creation of turbulence in the atmosphere are wind shear and buoyancy [4], with their relative importance differing among the categories introduced above. CAT, typically occurring at higher altitudes, can be triggered by Kelvin-Helmholtz instabilities [5,6] created by wind shear, the amplification, overturning and breaking of mountain waves [7,8], or in the vicinity of large convective clouds [9]. BLT can be induced by thermal updrafts in daytime convective boundary layers, strong wind shear, and mechanical forcing associated with complex terrain. LLT is usually caused by wind shear and obstacles on the ground, e.g., the local topography close to the airport in combination with buildings and higher surface vegetation [10].

Large-Eddy Simulation (LES) was originally proposed in the 1960s for simulating turbulent atmospheric flows [11]. In contrast to RANS (Reynolds-Averaged Navier-Stokes) based models, LES can explicitly resolve the dominant turbulent scales responsible for most of the stress and turbulent kinetic energy (*TKE*), making it an ideal tool for a proper turbulence characterization. With increasing computational capabilities, LES has nowadays become one preferred methodology for the simulation of turbulent flow in the ABL. This includes basic boundary layer studies for convective [12,13] and stable [14–16] stratification or terrain induced flows [17,18], as well as a wide range of atmospheric applications, e.g., related to wind energy [19–21], or pollutant transport and dispersion in urban environments [22,23]. LES simulations for air safety purposes are, in contrast, still rather sparse and often focus on the potential effects of vegetation and buildings on LLT affecting the runway [24–26]. One recent study [27] has applied an LES approach for a case study to provide realistic turbulence data as input for a flight simulator. The scale of turbulent eddies in the atmosphere ranges from a few centimetres to kilometres, among which the most damageable eddies are those with a dimension similar to and larger than the aircraft, i.e., in the order of several tens to several hundred meters [10,28,29]. The chosen grid resolution should therefore allow for an explicit calculation of those relevant eddies, while the smaller turbulent fluctuations will be treated by an appropriate subgrid-scale (SGS) scheme. This makes LES particularly suitable for turbulence modelling at a rather high spatial resolution at a relatively low computational expense.

During take-off and landing, BLT and LLT are of major importance and their estimation and forecast should therefore play a key role in the site selection and runway design of an airport, in particular in complex terrain. Large parts of Norway, in particular along the Western and Northern coast, are highly dependent on regional air traffic connections and many of those regional airports are located in rather complex terrain and thus widely exposed to orographically induced turbulence [30]. The Norwegian Meteorological Institute performs to date operational turbulence forecasts for several particularly exposed airports [31], based on the CFD code SIMRA [32]. However, the SIMRA model does not explicitly resolve turbulence, does not calculate buoyancy, and the spatial resolution of the operational runs is only 100 m.

We propose in this study a novel method for the systematic investigation of the surrounding of a planned airport in rather complex terrain by systematic LES modelling. A set of LES runs for 16 different wind directions and two different geostrophic wind speeds of 10 $ms^{-1}$ and 20 $ms^{-1}$ aims to map potential turbulence hot-spots in the vicinity of the new airport, in particular along the expected flight paths during landing and take-off. This information is expected to provide guidance and decision support for the location of the new airport and the corresponding flight route planning.

This paper is structured as follows. A brief introduction of the research site is presented in Section 2. The simulation software and the data analysis method are described in Section 3. Section 4 introduces the simulation results and discusses them in terms of wind speed and direction (Section 4.1), and the impact of atmospheric stratification (Section 4.2). Finally, a summary and conclusion, along with a short-term outlook of this study, are given in Section 5.

## 2. Study Area-Leknes, Lofoten Islands

Lofoten is an archipelago on the Northwestern coast of Norway, roughly located between 68 and 69° N (see Figure 1a). It stretches over ca. 120 km in the SW-NE direction and is characterized by complex topography, with the highest peaks exceeding an elevation of 1000 m. The largest airport in the Lofoten islands is Leknes airport (IATA: LKN), which is located in the Southwestern part of the island of Vestvågøy at 68°09′09″ N 13°36′34″ E. Its runway lies approximately along the SSW-NNE direction (RWY03-RWY21) and has a length of 891 m, limiting it for regional operations with rather small aircraft, e.g., the De Havilland Canada models Dash-1 and Dash-8. Avinor, the operator of 44 state-owned airports in Norway, is a wholly-owned state limited company under the Norwegian Ministry of Transport and Communications, is recently investigating potential locations for a new airport on the Lofoten islands [33], allowing for direct access to the region with larger commercial aircraft. During this process, one year of observations with multiple scanning wind lidar systems has been performed at selected locations. Anticipating the future data availability of those measurements for research purposes, in particular for the comparison with our model simulations, we have chosen Leknes airport as our study area.

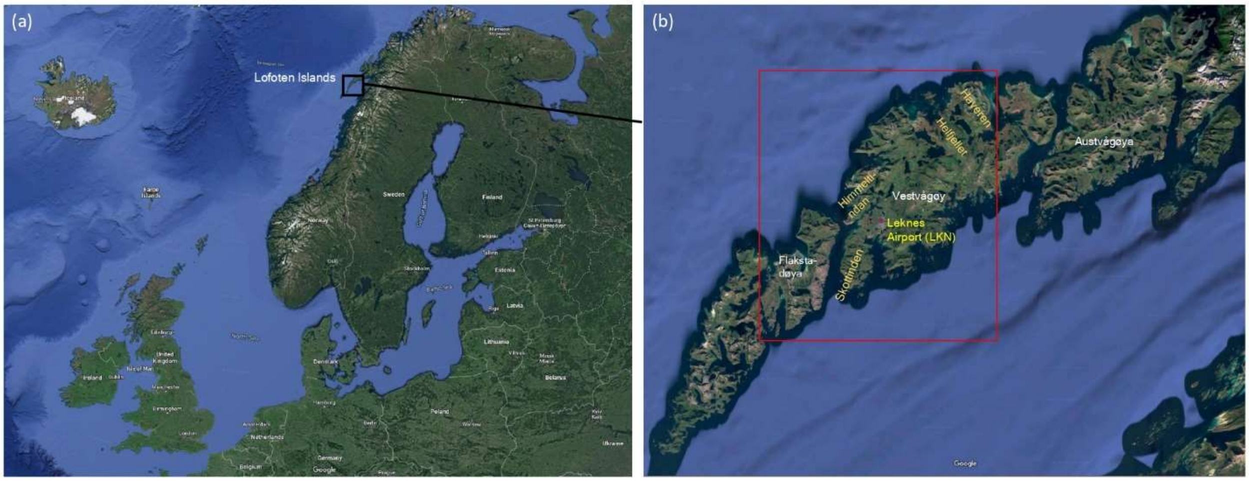


**Figure 1.** The location of the Lofoten archipelago on the coast of Northern Norway (**a**) and a zoom-in on the location of Leknes airport LKN on the island of Vestvågøy and its surrounding geography (**b**). The red box indicates the LES model domain used in this study. Credit: Google Map.

## 3. Materials and Methods

### *3.1. Simulation Setup*

#### 3.1.1. Simulation Model-PALM

Simulations for this work were performed with the PALM model version 6 revision 4579. PALM is an open-source, Fortran-based LES code, developed and maintained by the Institute of Meteorology and Climatology (IMUK) at the Leibniz University in Hannover, Germany. It is solving the spatially filtered, non-hydrostatic, incompressible Navier-Stokes equations using the Boussinesq approximation [34]. Advection terms are used in the prognostic equations and are realized by an upwind-based 5th-order differencing scheme [35] with a 3rd-order Runge-Kutta time-stepping scheme [36]. For parameterization of the eddies smaller than the grid spacing, PALM uses a subgrid-scale (SGS) model applying a 1.5th-order closure method following Deardorff 1980 [37], revised by Moeng and Wyngaard [38] and Saiki et al. [39]. This method is based on the hypothesis that the energy transport by SGS eddies is proportional to the local gradients of the mean quantities. For a detailed and general description of the PALM model, we refer to Maronga et al. [40,41]. PALM has been widely used in atmospheric boundary layer research for more than 20 years and numerous studies of the atmospheric boundary layer have been performed with this model [24,26].

#### 3.1.2. Simulation Suite and Parameters

Based on the parameter set as described in Table 1, we conducted two sets of simulations for two geostrophic wind speeds of 10 (Set10) and 20 $ms^{-1}$ (Set20). For each wind speed, simulations have been performed for 16 different wind directions (N, NNW, NW, WNW, W, WSW, SW, SSW, S, SSE, SE, ESE, E, ENE, NE, NNE), resulting in a total of 32 simulations. Every simulation output included hourly-averaged 3-D wind fields at every simulation hour. The *TKE* and wind distribution were analyzed for the whole computational domain.

**Table 1.** Summary of main parameters used in the simulation for this study.

| Name | Value |
|---|---|
| Grid resolution (dx, dy, dz) | 50 m |
| Grid points | $800 \times 900 \times 80$ |
| Simulated time | 12 h |
| Number of timesteps | 25,341 |
| CPU cores | 400 |
| RAM allocated | 32,768 MB |
| Initial surface sensible heat flux | 0.01 $Kms^{-1}$ |
| Zonal boundary condition | cyclic |
| Meridional boundary condition | cyclic |
| Vertical boundary condition | no-slip |

#### 3.1.3. Topography Data

The two-dimensional topography data was derived from the Norwegian Mapping Authority (Kartverket) [42,43]. The original dataset used the European Terrestrial Reference System 1989 (ETRS89) and the NN2000 altitude system. The datum was WGS89 and was in Digital Terrain Model with a grid resolution of 10 m (dtm10). The original data was block-averaged to fit the grid resolution of the corresponding LES simulation using MATLAB.

#### 3.1.4. Domain and Boundary Conditions

The simulations used cyclic boundary conditions in both west-east (x) and south-north (y) directions. This requires that cells near the boundaries of the domain are fluid cells. As the Lofoten islands spread along the southwest-northeast direction, a truncation of the topography had to be performed to match this criterion for the western and eastern boundaries. Such a truncation has to be carefully chosen so that it doesn't significantly affect the atmospheric flow near the LKN airport, as well as the numeric stability of integration at the boundaries of the domain. Ideally, the domain is chosen such that LKN is close to its centre, and the truncation of topography avoids steep gradients at the edge of the domain. What we need to avoid is that the potentially affected range in the downwind of the ridge on the boundary, expected to extend about 10 to 15 times of its altitude [44], will not disturb our area of interest around LKN. To achieve this, the horizontal size of the domain must be at least 2.5 times larger than this range in both directions [45,46]. Consequently, we chose for our study a rectangular simulation area between 13.17 and 14.04° E in longitude, and 68.00 and 68.36° N in latitude. The northern and southern boundaries lie completely in the ocean, the eastern boundary crosses the Lyndalsvatnet and the western boundary follows the Kåkersundet channel between the Flakstadøya and Moskenesøya islands. All boundaries were at least 19 km from LKN, and the steepest artificial edge by the truncation appears in the northwestern corner with an altitude of approximately 150 m. Thus, we are confident that our domain selection minimizes the effect of topography truncation. The scattered residuals and islands at the southwestern corner of the domain were also omitted. After the truncation, we end up with a rectangular box of $38.99 \times 42.73$ $km^2$ with LKN located near the centre of the domain, see the red rectangle in Figure 1b. However, the west and east edges of this domain still contain solid cells, and the size of this domain ($3899 \times 4273$) was not convenient for parallel computing, given the 400 cores we had on a high-performance computer (HPC) for simulations. Therefore, we added layers of fluid cells at all boundaries to fulfil the requirement of cyclic boundary conditions, as well as to make the number of grid points in every direction a multiple of 400.

In the vertical direction (z), the maximum height of the domain was set as 4 km. For the boundary conditions of potential temperature, a constant surface sensible heat flux was applied at the bottom, and the top sensible heat flux was calculated from the initial surface sensible heat flux and the initial potential temperature profile. For the boundary condition of horizontal velocity components, a no-slip condition was used at both the surface and the top of the domain. The final computational domain was chosen as the $40 \times 45 \times 4\,\mathrm{km}^3$ box shown in Figure 2.

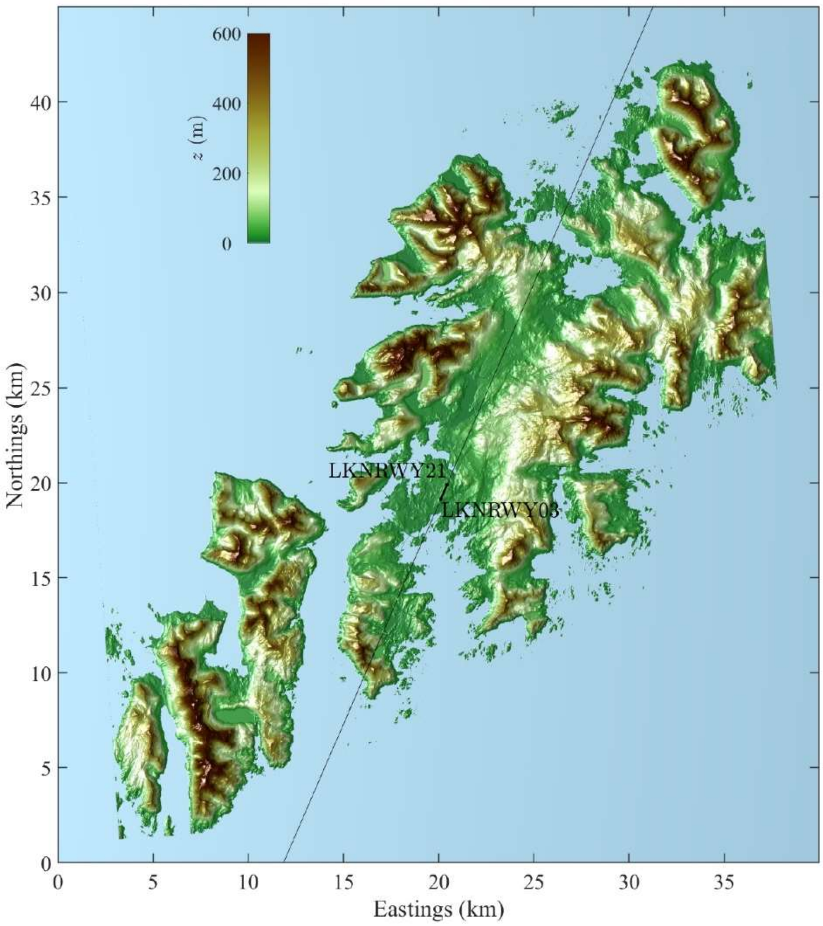


**Figure 2.** The topography map of the computational domain. Colours indicate altitude above sea level. The bold line indicates the current runway of LKN, with its southeastern end LKNRWY03 and northwestern end LKNRWY21. The thin line indicates the location of the vertical cross-section through the domain in the direction of the runway.

### 3.1.5. Sensitivity Analysis

Although being an effective software to perform LES simulations, the expenses of computational power for such an extended domain in PALM are still extensively high (see Table 2). All the simulations were conducted on the HPC facility Fram, operated and maintained by the Norwegian research infrastructure services (NIRS). In order to balance simulation performance and computational expense, it is necessary that the grid resolution, as well as the overall simulation period, are carefully determined and optimized by sensitivity tests before conducting the full set of simulations. Therefore, we chose grid resolutions of 25, 50 and 100 m, and ran the simulation with otherwise identical parameters and topography data. The simulation time was initially set to 12 h to make sure the simulations have enough time to converge and stabilize. The corresponding results are shown in Figure 3 and indicate that the increase in velocity variances and *TKE* over time flattens distinctly at around 9 h. The simulations show, as expected, a clear increase in *TKE* (black lines) for decreasing grid spacing. Here the main improvement takes place for a refinement of the grid from 100 m to 50 m. A further decrease in grid spacing to 25 m improves the performance with respect to *TKE* resolution only marginally, consumes, however, nearly 20 times more computational resources. Based on those results we have chosen to perform the further simulations for 12 h with a horizontal and vertical grid resolution of 50 m.

**Table 2.** Computational resource usage of one simulation in different grid resolutions. The simulated time was 12 h for each test.

| Grid Resolution | Avg. Simulation Time | Avg. Memory Usage | Avg. Disk Write |
|---|---|---|---|
| 25 m | 20:21:56 | 493 GB | 59 GB |
| 50 m | 01:15:36 | 141 GB | 7 GB |
| 100 m | 00:17:22 | 111 GB | 0.05 GB |

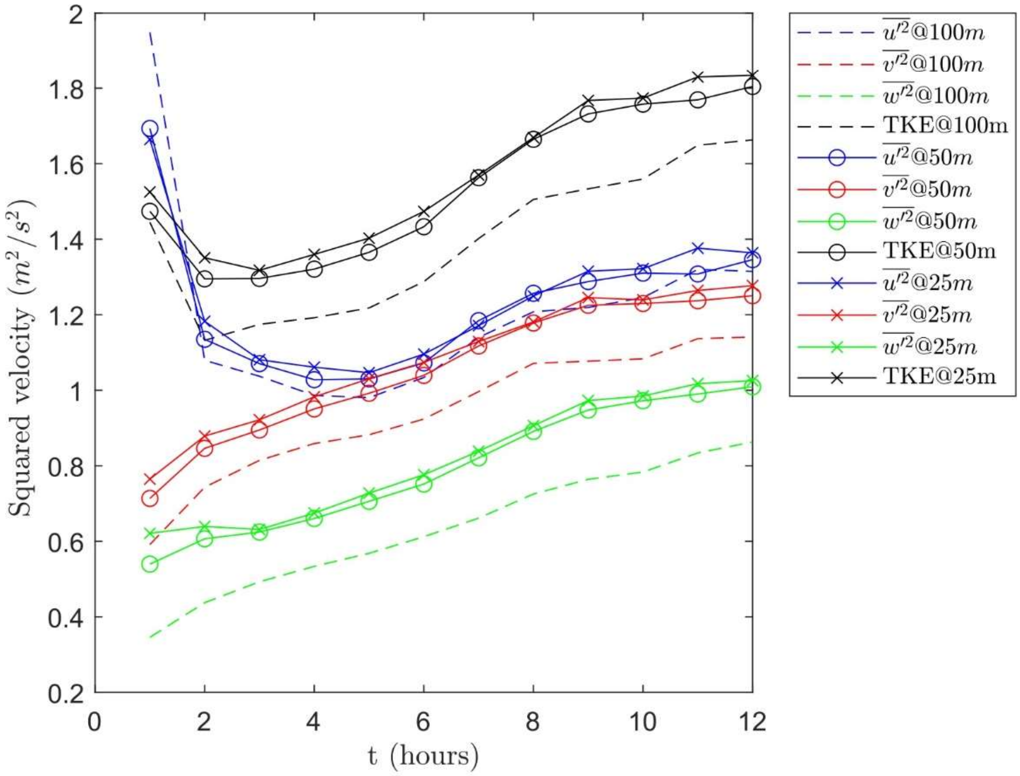


**Figure 3.** Comparison of mean resolved *TKE* and velocity variances for different grid resolutions (100 m, 50 m and 25 m).

### 3.2. Methodology

In our study, we investigate the three-dimensional characteristics of air-safety relevant BLT, with a particular focus on the conditions along the estimated glide paths during the final approach towards landing. The main proxy to represent the turbulence conditions in a computational region is the resolved *TKE*, i.e., the turbulent kinetic energy explicitly resolved and directly simulated by the model. At every hour in the PALM simulation, for a unit of air mass, hourly-averaged cardinal velocity components $(\overline{u}, \overline{v}, \overline{w})$ and squared cardinal velocity components $(\overline{u^2}, \overline{v^2}, \overline{w^2})$ were stored, and the hourly-mean resolved *TKE* was then calculated as:

$$TKE = \frac{1}{2}[(\overline{u^2} - \overline{u}^2) + (\overline{v^2} - \overline{v}^2) + (\overline{w^2} - \overline{w}^2)] \quad (1)$$

Note that the calculation in (1) is representing the resolved *TKE* per unit of air mass, so its dimension is J/kg, i.e., $m^2s^{-2}$.

The simplest meteorological variables considered most important for aviation safety are the *F*-factor [47], representing the wind shear ahead of the aeroplane, and the turbulence dissipation rate $\epsilon^{1/3}$. These quantities are given by the Equations (2) and (3):

$$F = \overline{-\frac{c}{g}\frac{\partial u}{\partial x} + \frac{w}{c}}^{l_f} = -\frac{c}{gl_f}[u(x + l_f/2 - u(x - l_f/2)t] + \frac{\overline{w}^{l_f}}{c} \quad (2)$$

$$\epsilon^{1/3} \approx \left(\frac{(C_\mu^{1/2}K)^{3/2}}{l_t}\right)^{1/3} \approx 0.67K^{1/2}l_t^{-1/3} \quad (3)$$

here $c$ is the flight path, $g$ is the gravitational acceleration, $\mu$ is the wind component along the flight path, $w$ is the vertical wind component, $K$ is *TKE*, $l_t$ is turbulent length scale and $l_f$ is the minimum response distance in landing configuration, which is of the order of ∼500 m, corresponding to a time interval of about $t = O(7\,s)$. The coefficient $C_\mu$ has a value of approximately 0.09. A comprehensive review of this theory is given in Eldsvik et al. [48]. Regions prevailed by the conditions $F < -0.1$ and $\epsilon^{1/3} > 0.5\ m^{2/3}s^{-1}$ correspond to severe turbulence for commercial aircraft and represent potential danger [49]. These conditions are easily met when $K^{1/2} > 3\ ms^{-1}$, so we chose 9 $m^2s^{-2}$ as the *TKE* threshold to distinguish locations with high turbulence risk in our study.

In the investigation of aviation safety, we aim to analyze the potential risk a pilot might encounter during the final approach and take-off. However, the realistic strategies differ in terms of weather and visibility conditions, especially for airports near complex terrain. As a simplified model, we defined a 3-degree aircraft glide slope at both ends of the LKN runway to represent the approximate trajectory of an aircraft in our study [50]. In terms of aircraft landing, this model is very close to the realistic landing approach. For take-off, this model is less precise as the pitch slope of the aircraft varies from 3–12 degrees depending on the size of the aircraft, but still makes sense in analyzing the altitudes where high turbulence risk occurs near the airport. In addition, an aircraft during the start of take-off is considerably less vulnerable to the effect of terrain induced turbulence.

Based on this flight path model, turbulence hazard risks were then analyzed for all simulations. For each scenario, data selection along the flight path was done as follows: (1) coordinates of the intersections between the glide path and all the south-north surfaces were derived, (2) for each intersection, 4 adjacent grid points were collected as sample points. The sample points were then categorized according to *TKE* values and locations (RWY03 or RWY21), and the frequency of grid cells exceeding the *TKE* threshold was calculated to quantify the overall potential of turbulence hazard in each scenario.

## 4. Results

The main part of this study is dedicated to the spatial characterization of potentially dangerous situations of terrain induced BLT, dependent on wind speed and wind direction. In the following, we will present and discuss the simulation results of resolved *TKE* in the form of horizontal cross-sections at different altitude levels over the whole domain, the vertical cross-section defined by the orientation of the existing runway of LKN, and spatial profiles of *TKE* along the aircraft glide path during landing. To simplify the notations, in the remainder of the manuscript, the different model runs will be identified by the abbreviation of the wind direction, followed by the number of the corresponding wind speed. For example, the simulation with a 20 $ms^{-1}$ northwestern geostrophic wind is abbreviated as "NW20".

### *4.1. Atmospheric Stratification*

In PALM, the atmospheric stratification is determined by the wind speed and the sensible heat flux at the bottom surface [51]. To investigate its effect on the turbulence simulations, we selected 3 heat flux cases: (a) 0.01 $Kms^{-1}$, indicating near-neutral conditions; (b) 0.1 $Kms^{-1}$ representing moderately convective conditions and (c) 0.3 $Kms^{-1}$ for strongly convective conditions. Otherwise identical simulations of these 3 scenarios were performed for a geostrophic wind of 20 $ms^{-1}$ from Northwest (NW) and the resulting profiles of the resolved *TKE* along the glide path are presented in Figure 4. The profiles show highly variable *TKE* values including several terrain induced peaks, with three of them exceeding the threshold of 9 $m^2s^{-2}$. The maximum peak, in a distance between 5 and 10 km from the airport, reaches even above 25 $m^2s^{-2}$, indicating severe BLT conditions induced by the terrain. However, the profiles for the different stability conditions are very similar in shape and absolute value and indicate that atmospheric stability plays only a secondary role in the creation of terrain-induced *TKE*. Thus we have chosen to only use the heat flux value of 0.01 $Kms^{-1}$ further on in this study.

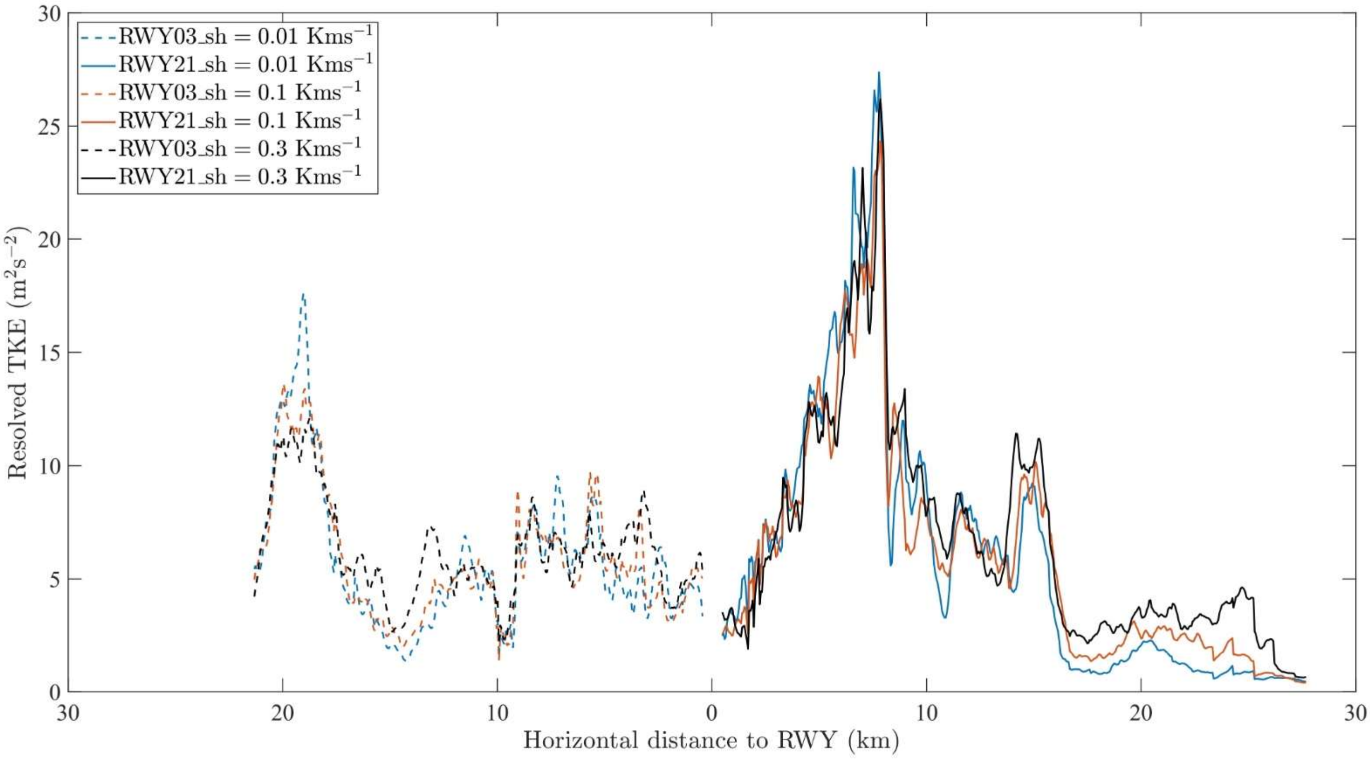


**Figure 4.** Profiles of resolved *TKE* along the aircraft glide path under three atmospheric stratification scenarios. Solid lines refer to RWY21, dashed lines refer to RWY03.

### *4.2. Turbulence Characteristics as Function of Wind Speed and Direction*

#### 4.2.1. Horizontal Cross-Sections

The horizontal wind field and resolved *TKE* field were analyzed for the complete area of interest at the three heights of 100 m, indicating the layer LLT appears, 500 m and 1000 m, roughly the level of the highest mountain tops. The key features of selected simulations are described in the following section, while the corresponding plots of all simulations are available in the Appendix A (Figures A1 and A2).

Figure 5 presents the results for the simulations with a geostrophic wind from NW of 10 $ms^{-1}$ and 20 $ms^{-1}$ (cases NW10, left panel and NW20, right panel) at an altitude of 100 m. NW10 shows over the whole model domain considerably lower *TKE* values than NW20, indicated by the darker blue colour. There is an indication of weak terrain induced turbulence in the lee of the mountains, the *TKE* threshold of 9 $m^2s^{-2}$ is, however, hardly reached or exceeded in this run. The simulations for NW20 show, in contrast, distinct maxima in the *TKE* field that exceed the threshold nearly everywhere on the lee side of the topography. Those patches of heavy terrain-induced turbulence extend typically for at least 5 km downwind from the initiating mountain ridges, before gradually dissipating. No significant signal was found near the airport runway in either case, and the turbulence condition in the valley of Vestvagøy was only moderate. This indicates a relatively low probability for an aircraft experiencing LLT related safety issues at this level.

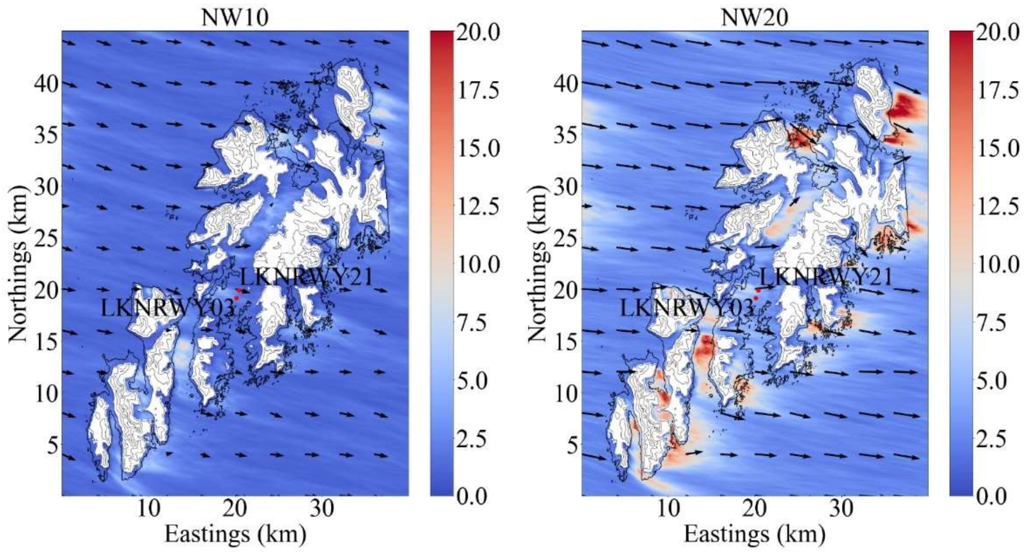


**Figure 5.** Horizontal resolved *TKE* ($m^2s^{-2}$) and wind conditions at 100 m height for geostrophic wind from NW with 10 $ms^{-1}$ and 20 $ms^{-1}$ (cases NW10 and NW20). The color shading indicates the resolved *TKE*, the black arrows represent wind speed and direction, and the grey lines indicate the contour lines of the topography. The color scale is chosen in a way that the transition between blue and red corresponds to the *TKE* threshold of 9 $m^2s^{-2}$.

One feature worth noticing in the horizontal cross-section plots is the turn of wind direction relative to the geostrophic wind. In NW20, the wind direction at 100 m height is more or less purely west, indicating a counter-clockwise turn of 30–40° from its geostrophic start value. This can be explained by the effect of surface friction within the Ekman layer, resulting in ageostrophic and cross-isobaric winds inside the ABL.

Figure 6 presents exemplary results for the simulations with a 20 $ms^{-1}$ geostrophic wind from NW (left column, NW20) and NE (right column, NE20) for three different ABL levels of 100 m (top plots), 500 m (center plots), and 1000 m (bottom plots). The full set of simulations for the three altitude levels can be found in Appendix A (Figures A2–A4). The NW case shows in general overall slightly higher *TKE* levels and correspondingly also larger areas affected by strong turbulence above the *TKE* threshold level. This indicates that the effect of the orientation of the topography with respect to the wind direction plays an important role. The highest *TKE* levels for both wind directions are observed in the cross-sections at 500 m altitude, more or less corresponding to the average altitude of turbulence inducing terrain features in the free flow. At 1000 m only the highest peaks can contribute to corresponding disturbances, and their abundance is therefore considerably reduced. Compared to the 100 m level, the higher cross-sections indicate also a clearly increased downwind extension of the turbulent patches, often exceeding 10 km from their origin.

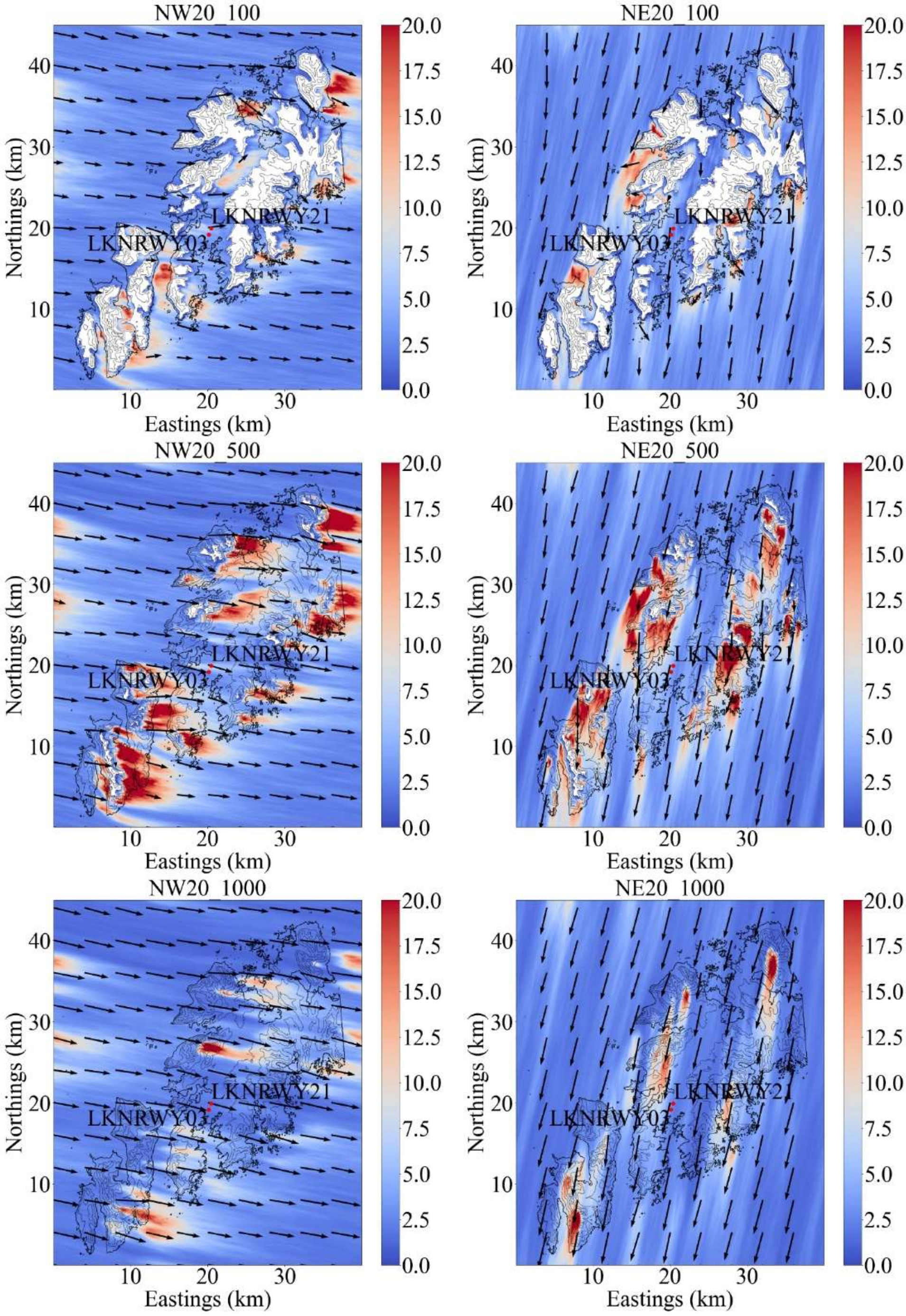


**Figure 6.** Horizontal resolved *TKE* ($m^2s^{-2}$) and wind conditions at 100 m (upper panels), 500 m (middle panels), and 1000 m (lower panels) for a geostrophic wind of 20 $ms^{-1}$ from NW (left panels, case NW20) and NE (right panels, case NE20). The color shading indicates the resolved *TKE*, the black arrows represent wind speed and direction, and the grey lines indicate the contour lines of the topography.

#### 4.2.2. Vertical Cross Sections

The vertical resolved *TKE* field was also analyzed at the vertical cross-section in the direction of the LKN runway from the surface to 1500 m. Plots of all simulations for 10 $ms^{-1}$ and 20 $ms^{-1}$ are available in Appendix A (Figures A5 and A6). Figure 7 illustrates the distributions of *TKE* for the NW20 and NE20 cases, the glide slopes are indicated by the thin black lines. In correspondence with the findings presented in Figure 6, we can observe a clear discrepancy in the amount of resolved *TKE* between these two cases. In NW20, there are three turbulence hot spots intersecting with the glide slope, one in the direction of RWY03, and the two others along RWY21. The maximum is observed at a distance of approximately 5km from LKNRWY21, and its intersection with the glide slope is at around 400 m height. By referring to the topography, we can associate this maximum with the hills next to LKN to the north. This maximum in NW20 extends to around 1000 m and quickly fades until above 1200 m, in correspondence with the initializing peak Himmeltindan of 982 m height. In contrast, the general situation of resolved *TKE* in NE20 is low to moderate, with only one area of slightly enhanced *TKE* at about 10 km south of LKNRWY03, located in the lee of the hills next to LKN in the south. A possible explanation for such discrepancy is the difference of orographic form drag the flow experiences [52,53], dependent on the orientation of the turbulence initiating terrain relative to the wind direction. In addition are the upstream flow conditions different for the two chosen wind directions. For NW20, wind travels only above the ocean before reaching the hills, thus most of its kinetic energy is preserved, providing more energy available for generating turbulent eddies. For NE20, on the other hand, the wind has crossed over tens of kilometres of mountainous area when reaching the hill, and parts of its kinetic energy has been dissipated due to frictional effects. This general difference in wind speed can also be observed in Figure 6, where the leeward created *TKE* in NE20. With significantly reduced wind speed, the *TKE* generated in the leeward becomes less accordingly.

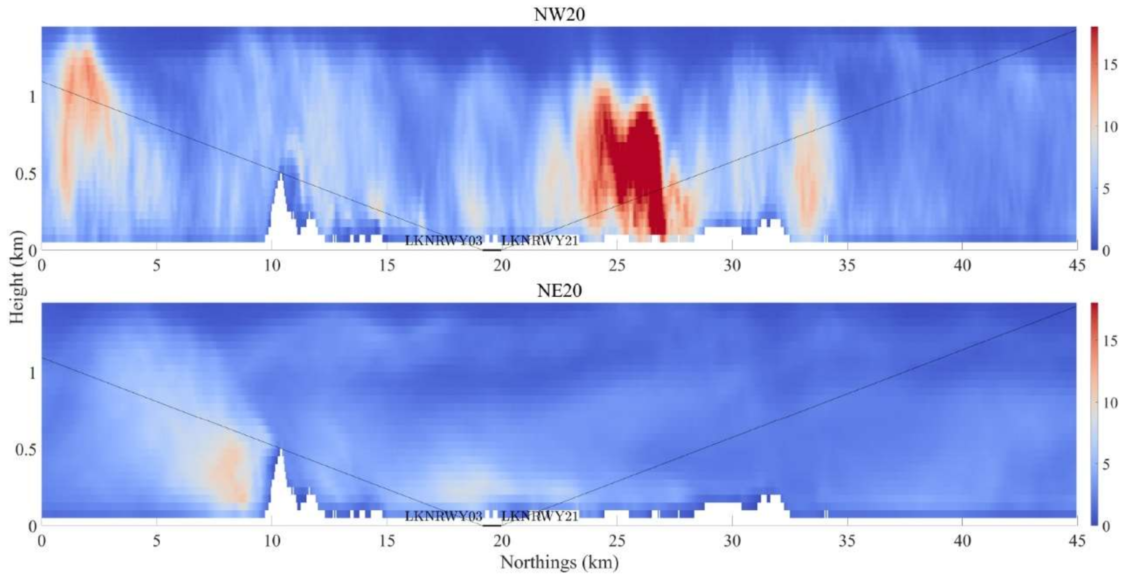


**Figure 7.** Map of resolved *TKE* ($m^2s^{-2}$) and wind conditions of NW20 and NE20. Color shade indicates resolved *TKE*, the solid line at the surface indicates the current LKN runway with ends LKNRWY03 and LKNRWY21, thin lines indicate the aircraft glide slope.

### 4.3. Aviation Safety Risk Analysis on the Glide Slope

For an estimation of the potential of turbulence encounters in flight, we present spatial *TKE* profiles along the slanted gliding path. As explained before, we have in this study chosen a hypothetical constant glide angle for this purpose. With the availability of more detailed flight route information for start and landing in the future, our method can be easily adapted. Figure 8 shows the turbulence distribution along the glide slope for all simulations, illustrating the potential turbulence risks and locations an aircraft might encounter during start and landing. Dashed lines correspond to the simulations with a geostrophic wind speed of 10 $ms^{-1}$ (set10), solid lines to ones of 20 $ms^{-1}$ (set20). The different colours indicate the direction of the two glide paths originating from LKN airport, in blue the one towards NNE (LKNRWY03) and in red the one towards SSW (LKNRWY21). For set10 the threshold of 9 $m^2s^{-2}$ is never exceeded for any of the 16 different wind directions. Consequently, air safety related issues due to terrain induced BLT are not to be expected for wind speeds below and around 10 $ms^{-1}$. For most of the wind directions of set20, with exception of two (S and NE), one or several peaks in *TKE* exceed the threshold, giving a clear indication that terrain induced turbulence provokes a common and considerable aviation risk near LKN when the wind speed approaches 20 $ms^{-1}$. Fortunately, none of those peaks are situated in the near-surface region close to the runway, meaning that it is not likely for an aircraft to encounter strong turbulence at very low altitudes close to touchdown.

For a quantitative comparison of the related risks, a statistical analysis of the turbulence conditions along the glide slope was performed, following the methodology described in Section 3.2. The probability of high turbulence risk is expressed by the frequency of occurrence of extreme *TKE* values along the glide path, calculated as the ratio of grid cells exceeding the 9 $m^2s^{-2}$ threshold to all grid cells along the glide path. The results of this analysis are summarized in Figure 9. Among the 16 cases in set20, the most turbulent one is NW20, with 17.3%, while the least turbulent case is NE20, which doesn't have a single high-risk case. The highest peak in the RWY21 direction is also found in NW20, which is the maximum of above 25 $m^2s^{-2}$ we discussed in Section 4.2.2. The highest *TKE* value in the RWY03 direction is found in SW20, which is related to the hills in the south of LKN. By cross-comparing the profiles, we notice that the cases under adjacent geostrophic wind directions share similar features in the locations and magnitude of *TKE* peaks, so it is logical to discuss them in groups.

1. Southwesterly group (S20, SSW20, SW20, WSW20): The overall resolved *TKE* condition of this group is moderate, with a high turbulence probability of 3.6%. For the direction of RWY03, main peaks are observed in the lee of Skottind. For RWY21, only one high-risk area is found in SSW20.
2. Northwesterly group (W20, WNW20, NW20, NNW20): This group reports considerably more turbulence hot spots than the others, with a high turbulence probability of 14.1%. According to the profiles, there are two common hot spots along the RWY03 slope, and another two along the RWY21 slope. If we assume an aircraft is approaching along the RWY03 slope, it will first encounter intensive turbulence at approximately 750 m altitudes. This hot spot is located at the lee of the mountains on Flakstadøya. The mountains there run north to south, maximizing the blockage effect on northwesterly winds, and, as a result, generating high turbulence levels. The aircraft will cross high turbulence again at about 400 m in altitude. As discussed in Section 4.2, this hot spot is related to the mountains to the south of LKN.
3. Northeasterly group (N20, NNE20, NE20, ENE20): The high turbulence risk of this group is, 3.6%, again, moderate. Unlike the other groups, whose extreme values distribute relatively evenly, most of the extremes in this group are found in the major peak of ENE20. This peak stands out at about 20 km distance from RWY21, located above two lakes (Urvatnet and Steirapollen), situated between the mountains Helfjellet and Haveren. As discussed in Section 4.2.1, the wind field here turns northeasterly, maximizing the interference with Haveren. As a result, high turbulence levels are induced in the downwind region. The mechanism and wind setting of NE20 is quite similar, but the statistics yield results with huge contrast. By investigating the turbulence distribution for the whole domain, one can observe that the total amount of resolved *TKE* between NE20 and ENE20 is rather similar. However, due to the slight shift in wind direction, the turbulence hot spot induced by Haveren, moves slightly southeastwards to the lake Alstadpollen, making it undetectable in the cross-section along the LKN runway.
4. Southeasterly group (E20, ESE20, SE20, SSE20): This group is least overall least exposed to turbulence risks among the four groups, with a high turbulence probability of 2.1%. There are no shared peak locations among the group members, instead, various extreme values (with relatively low magnitude) spread in the region 10–20 km away from RWY21, i.e., the northeastern part of the main valley on the Vestvågøya island. The potential reason this group experiences the least turbulence risk is the fact that the topography on the southeastern side of Vestvågøya is lower and gentler than

its northwestern counterpart, but spread more continuously. Therefore, as the easterly winds in this group interfere with the mountains, turbulent eddies are induced in a larger area but with overall lower *TKE* intensity.

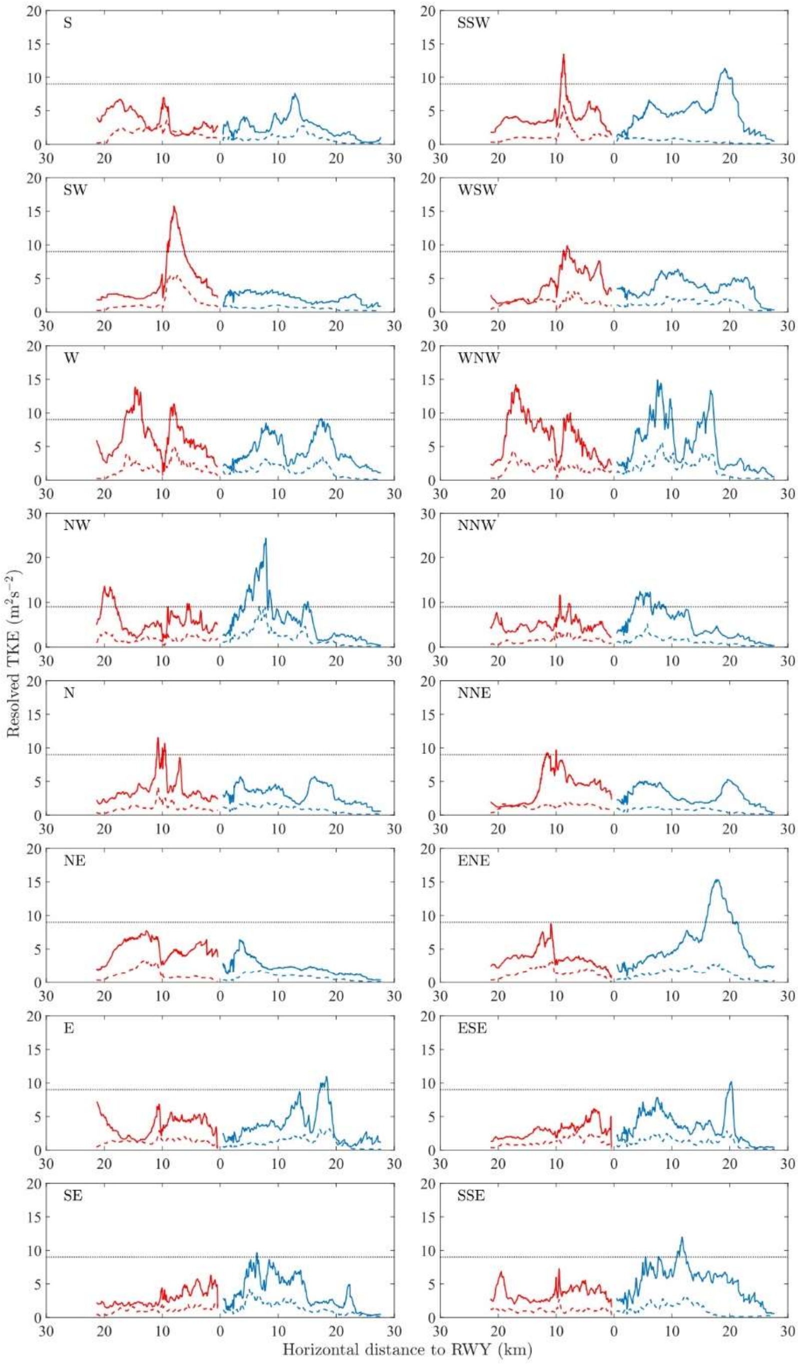


**Figure 8.** Profiles of resolved *TKE* along the aircraft gliding path of set20 (solid) and set10 (dashed). Blue lines indicate the slope in the direction of RWY03, and red lines indicate the slope in the direction of RWY21. The dotted lines indicate the 9 $m^2s^{-2}$ high turbulence risk threshold. Note the different ranges for the y-axis in the NW and NNW cases. The x-axis only denotes the horizontal distance between a point on the glide slope and its respective runway end, there is also an elevation of approx. 50 m for every 1 km horizontal distance.

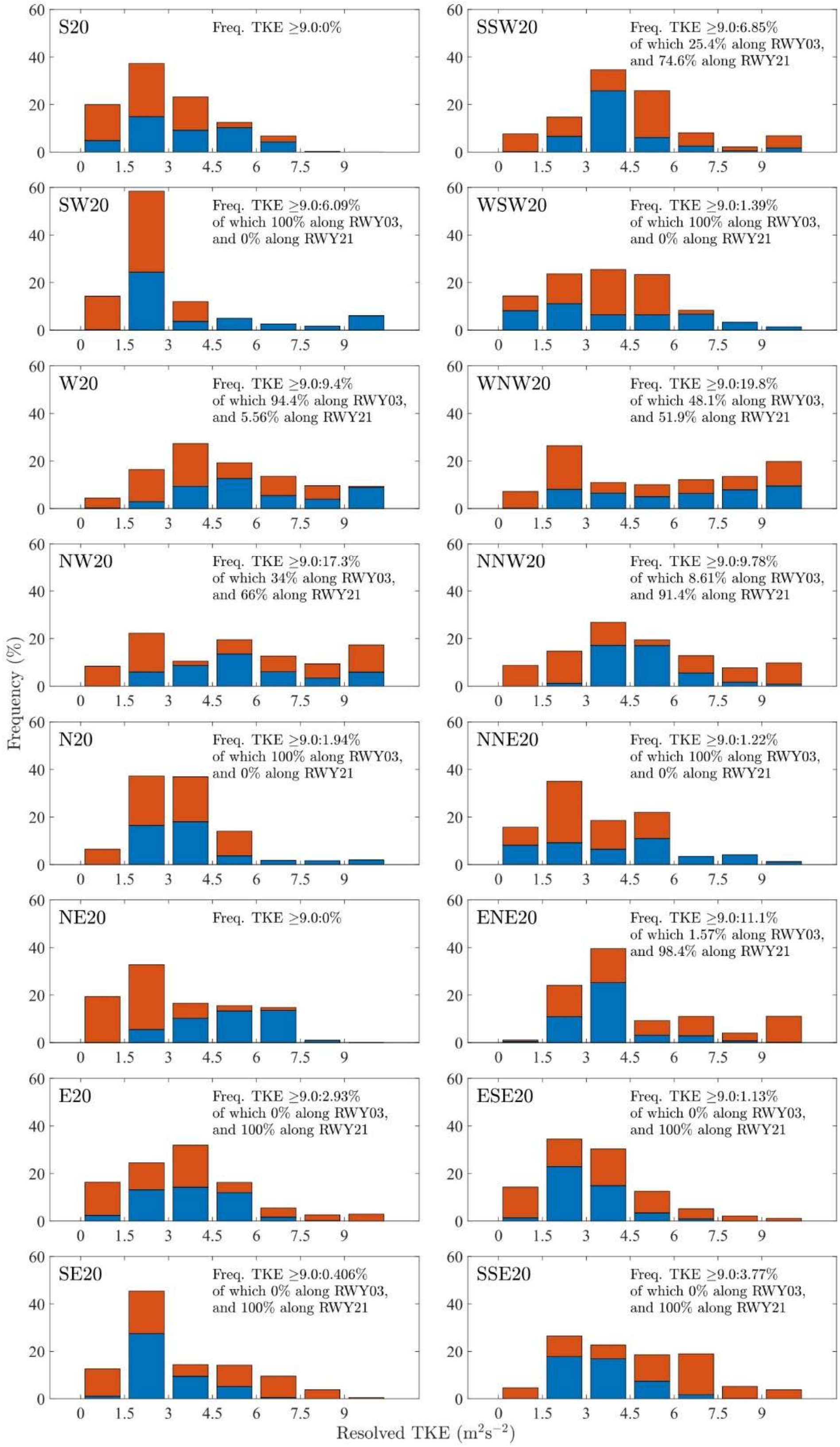


**Figure 9.** Distributions of resolved *TKE* along the glide slope in set20. Blue bars indicate cases on the RWY03 slope, orange bars indicate cases on the RWY21 slope. For each case, the probability of high turbulence risk and its composition are commented in the respective plot.

## 5. Conclusions and Outlook

This study investigates the turbulence conditions in the surroundings of the existing Leknes airport in the Lofoten islands. We studied the terrain-induced turbulence in the atmospheric boundary layer and performed a turbulence risk analysis on an idealized aircraft trajectory with respect to different geostrophic wind speeds and directions. To achieve these goals, a suite of simulation runs was carried out using the LES model PALM, based on a high-resolution topography dataset near the LKN airport in the Lofoten islands. Based on initial parametric sensitivity studies we have finally chosen a grid spacing of 50 m and a simulation time of 12 h for a suite of model simulations for 16 different wind directions and two geostrophic wind speeds of 10 $ms^{-1}$ and 20 $ms^{-1}$. The results show that PALM can properly simulate the turbulent flows for air safety related investigations in an extended domain with high resolution at an acceptable computational expense.

According to the simulation results of the wind field and turbulence in the whole domain, we demonstrated that the topographically-induced turbulence occurs in the lee of steep mountains and ridges. Those terrain-induced turbulence patterns extend typically 5 to 10 km downstream, with an indication of a slight increase in this extension with altitude. The highest *TKE* levels are observed in the middle of the ABL around 500 m altitude, more or less corresponding to the level of turbulence inducing terrain features in the free flow.

A turbulence risk analysis along idealized flight trajectories shows that the turbulence risk conditions are substantially determined by the wind conditions and their interaction with the topography. With respect to wind speed, the results indicate that for a geostrophic flow below 10 $ms^{-1}$, the risk of aviation critical, terrain-induced BLT, is rather low in the vicinity of LKN. At 20 $ms^{-1}$ the situation has completely changed and the aviation critical threshold of 9 $m^2s^{-2}$ is exceeded for 14 out of 16 of the investigated wind directions. Two main factors influence the observed directional dependency of the turbulence risk, one being the orientation of the topography with respect to the wind direction, and the fetch, i.e., the average upstream surface characteristics. Turbulent eddies in the lee form are particularly efficient when the flow intersects almost perpendicularly with the steep topography. The orographical form drag also plays an important role, as it affects the average wind speed of the upstream flow. The main topographic features are SW to NE oriented, with an average altitude decreasing from NW to SE. However, the southwestern mountains, mainly on Flakstadøya, run north to south. From the profiles and statistics we observed, for the southwestern glide slope RWY03, the highest turbulence risk occurs under westerly winds, and for the northeastern glide slope RWY21, the highest turbulence risk is associated with northwesterly wind.

This study presents a novel methodology as it uses for the first time a systematic LES modelling approach for the investigation of the turbulence characteristics for two geostrophic wind speeds and 16 different wind directions. Although the simulations already cover a considerable range of relevant meteorological conditions for the operation of a future airport, this study comprises still a limited subset of cases, in particular for higher wind speeds from critical wind directions. This is, however, beyond the scope of this proof-of-concept study. It should also be emphasized that the choice of aircraft trajectories in this study is rather idealistic. Nevertheless, it already provides a very good indication of the aviation relevant BLT risks in the vicinity of LKN. The design of our method allows, in addition, for an easy adaptation as soon as more detailed flight route information for take-off and landing will be available in the future.

A next natural step in the extension of this study would be a case study based comparison of the LES results with remotely sensed wind fields, e.g., collected by scanning Doppler-lidars [26,54] or acoustic soundings [55] in the area. This could be accomplished by either getting access to an already existing data set from Avinor, or by designing and performing a new and targeted measurement campaign that would, in the context of instrument placement and scanning patterns, highly benefit from the now available LES data set.

**Author Contributions:** Conceptualization and design of the model simulations, S.W., F.D.R., L.T. and J.R.; execution of the simulations, S.W. and F.D.R.; data analysis, S.W., F.D.R., L.T. and J.R., writing of first manuscript draft, S.W., internal review and finalization of the manuscript S.W., F.D.R., L.T. and J.R. All authors have read and agreed to the published version of the manuscript.

**Funding:** This study is funded as part of the EU project LIKE (Lidar Knowledge Europe) H2020-MSCA-ITN-2019, Grant number 858358.

**Institutional Review Board Statement:** Not applicable.

**Informed Consent Statement:** Not applicable.

**Data Availability Statement:** The LES data set forming the basis of this study is available from the corresponding author, [S.W.], upon reasonable request.

**Acknowledgments:** The LES simulations were performed on resources provided by UNINETT Sigma2—the National Infrastructure for High Performance Computing and Data Storage in Norway, under project number NN9506K.

**Conflicts of Interest:** The authors declare no conflict of interest.

## Appendix A. Figures of Full-Set Simulation Results

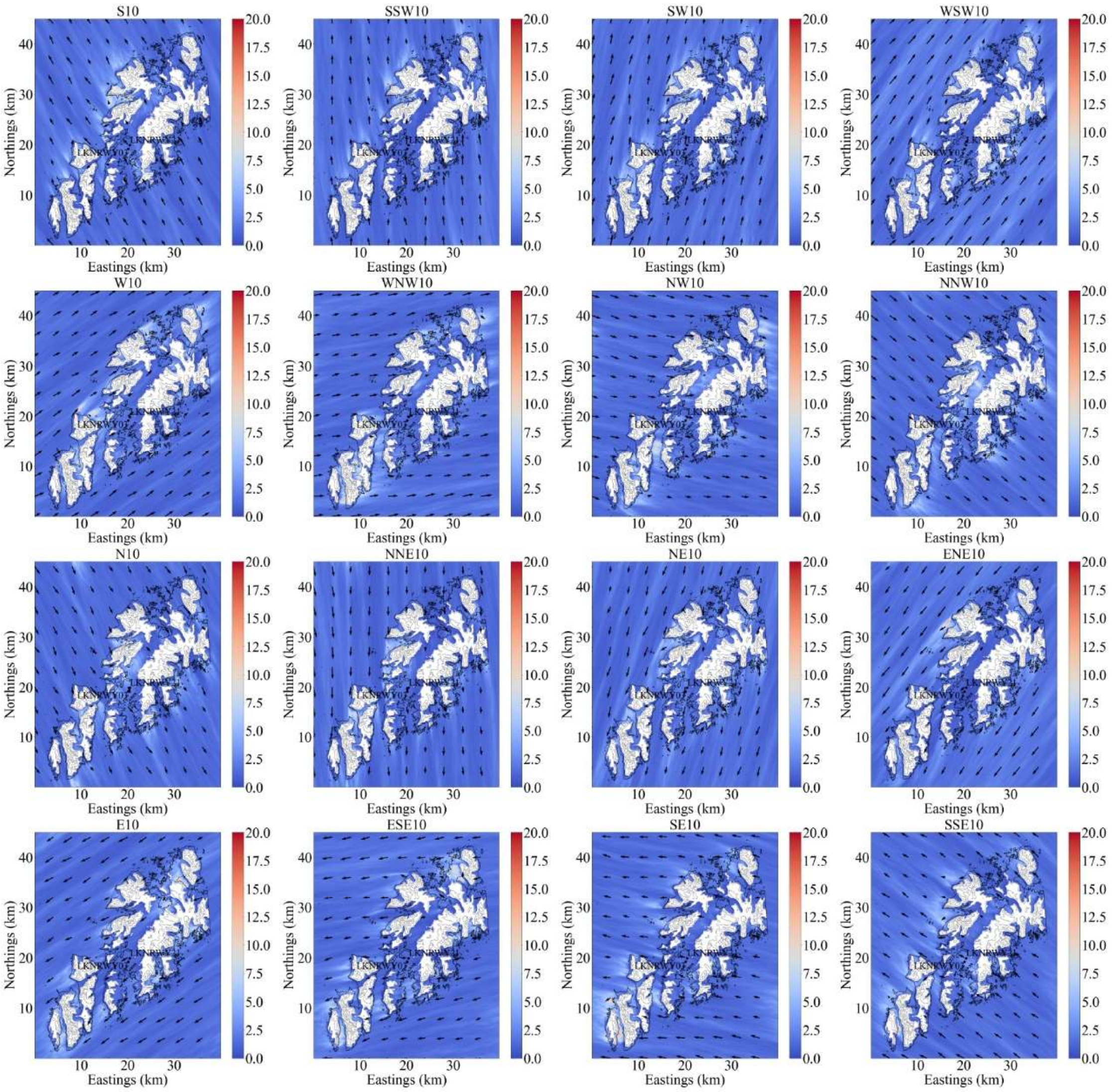


**Figure A1.** Horizontal wind and turbulence conditions ($m^2s^{-2}$) for the simulations of set10, z = 100 m.

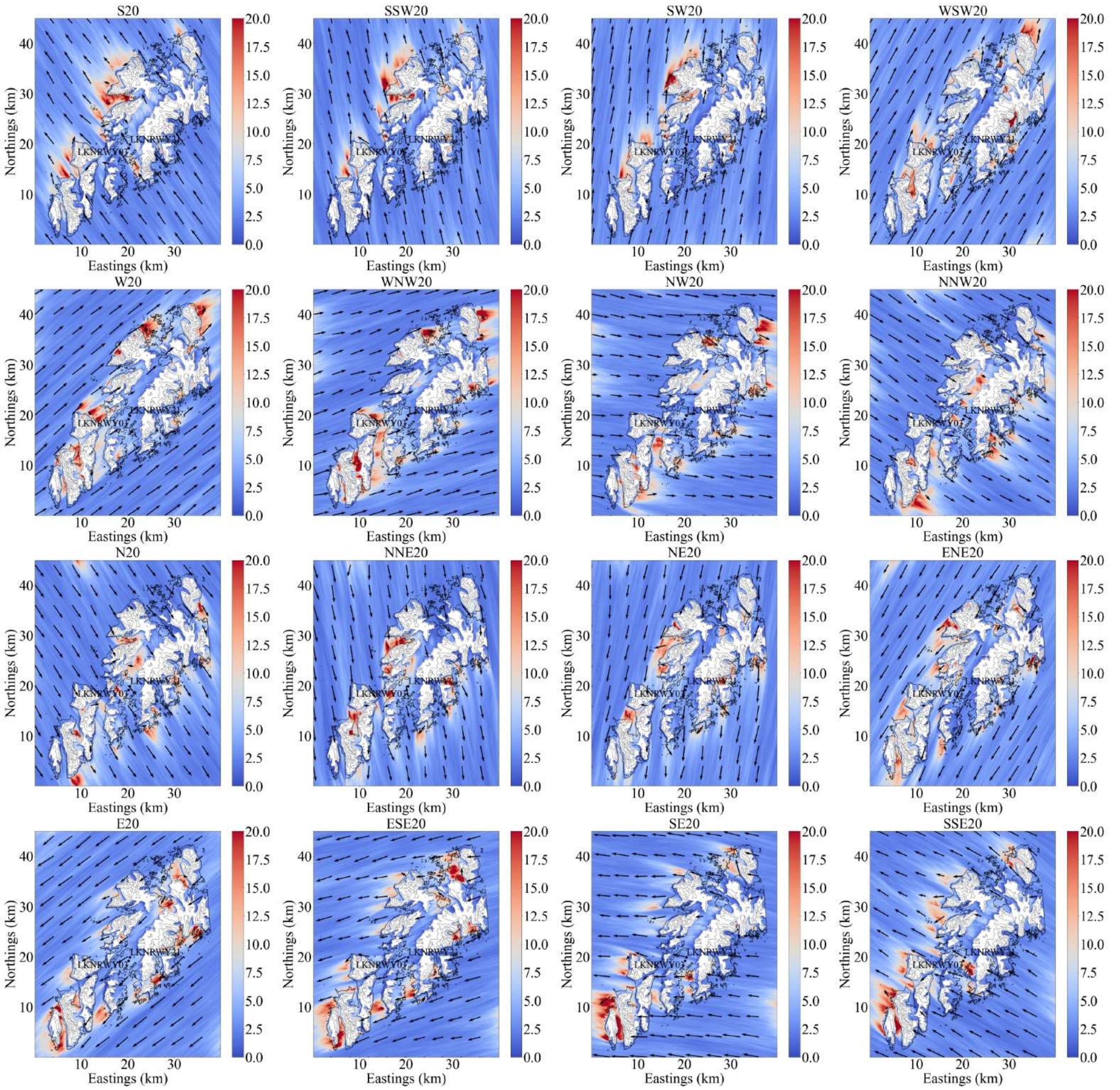


**Figure A2.** Horizontal wind and turbulence conditions ($m^2s^{-2}$) for the simulations of set20, z = 100 m.

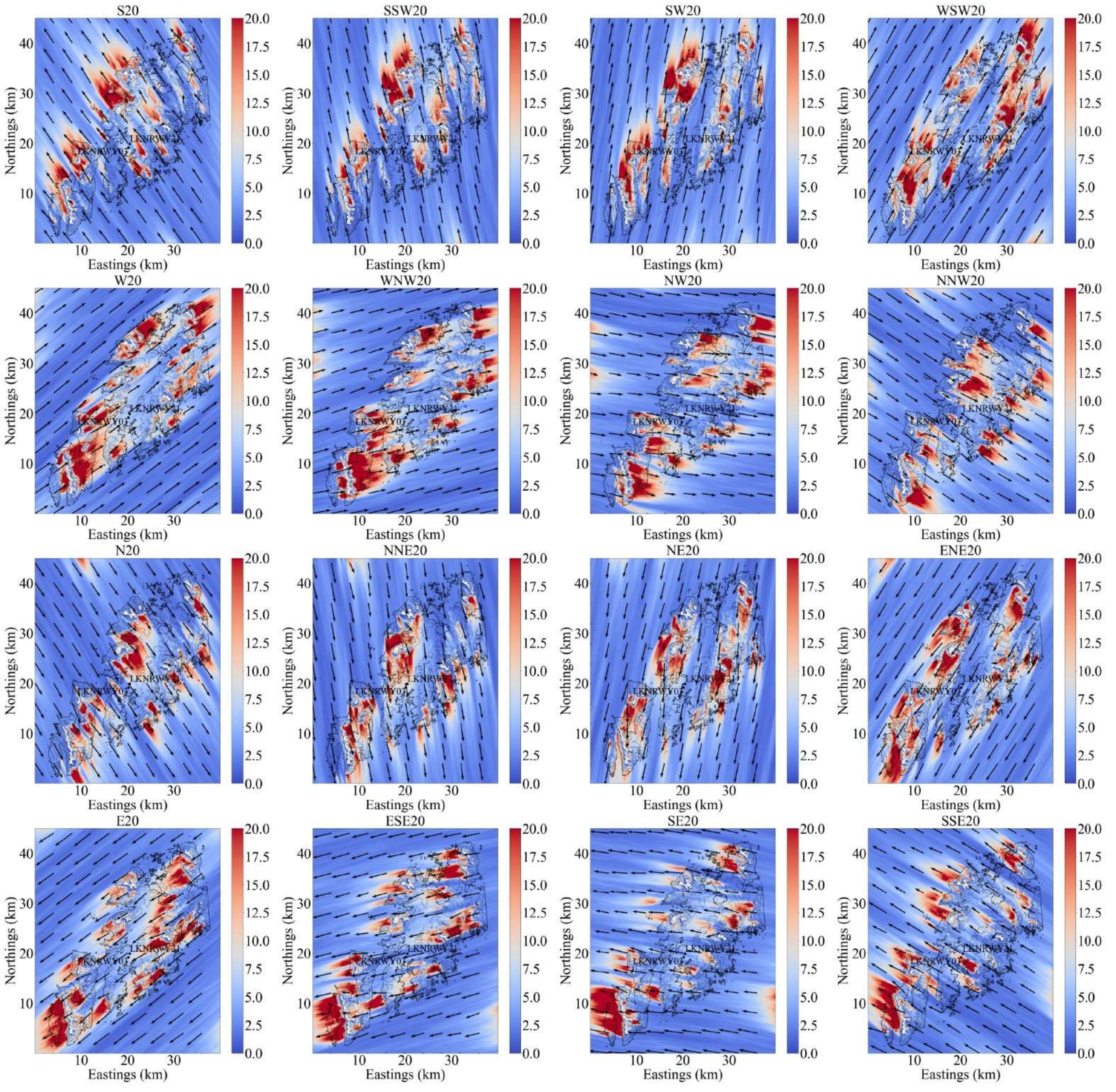


**Figure A3.** Horizontal wind and turbulence conditions ($m^2s^{-2}$) for the simulations of set20, z = 500 m.

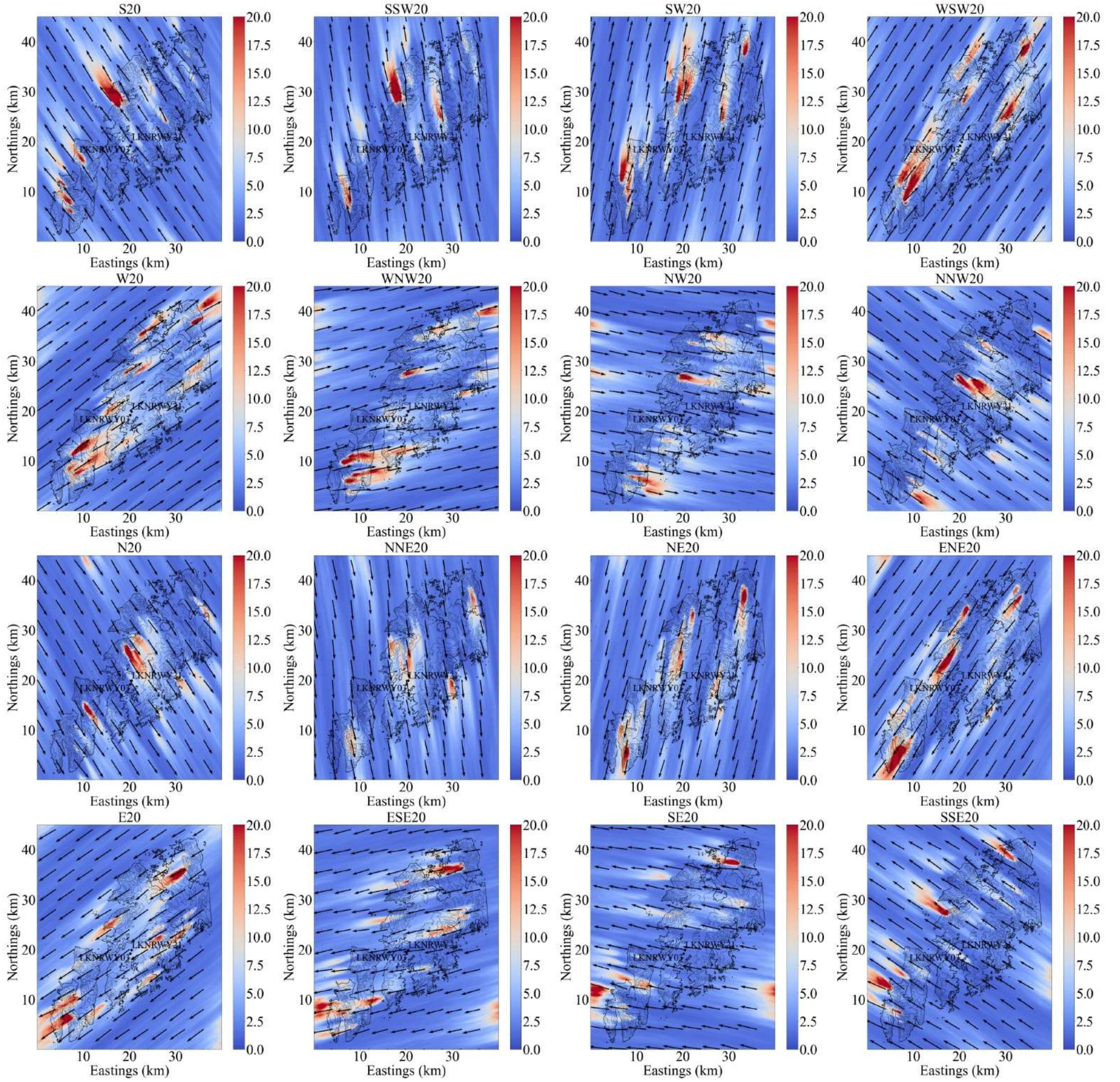


**Figure A4.** Horizontal wind and turbulence conditions ($m^2s^{-2}$) for the simulations of set20, z = 1000 m.

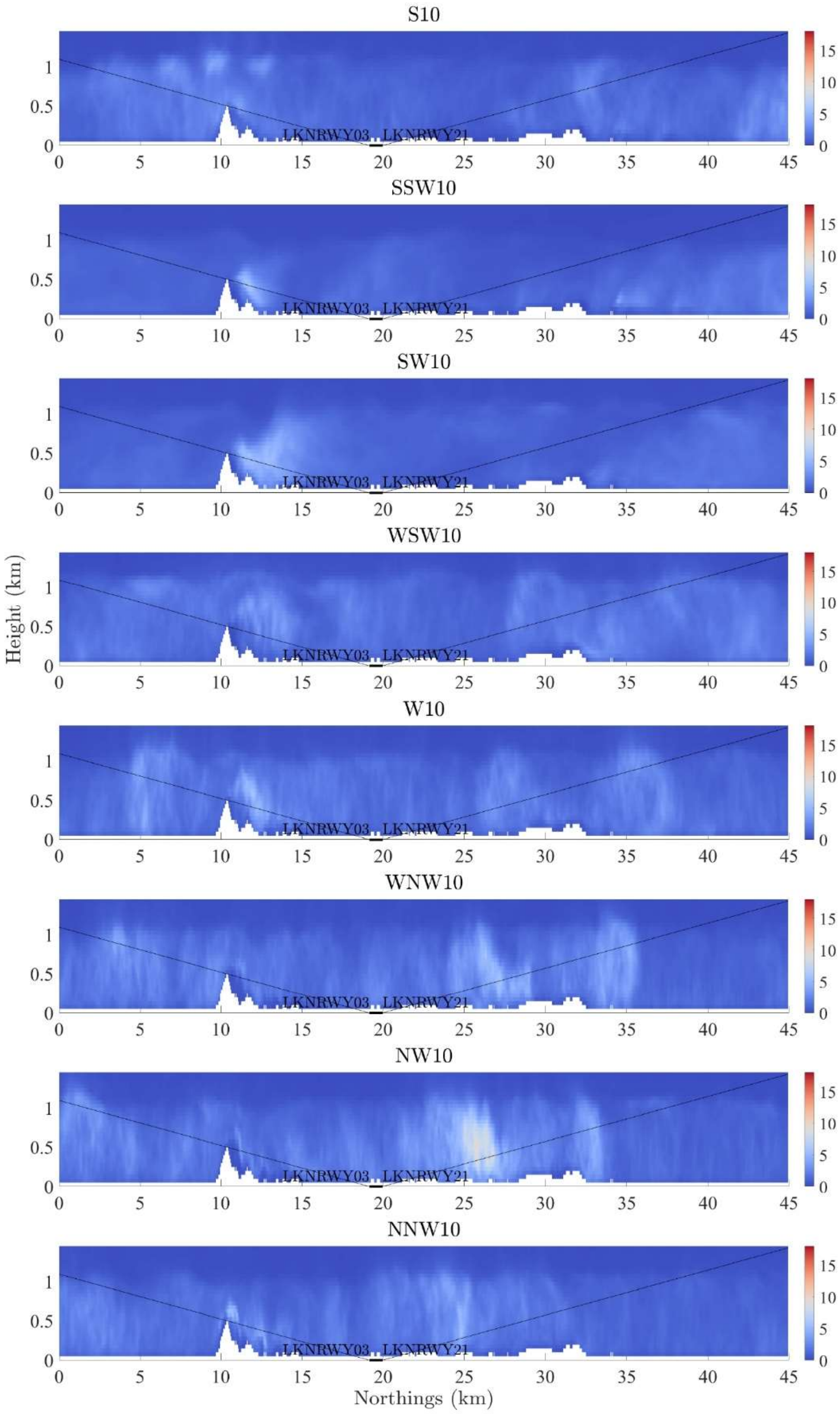


**Figure A5.** *Cont*.

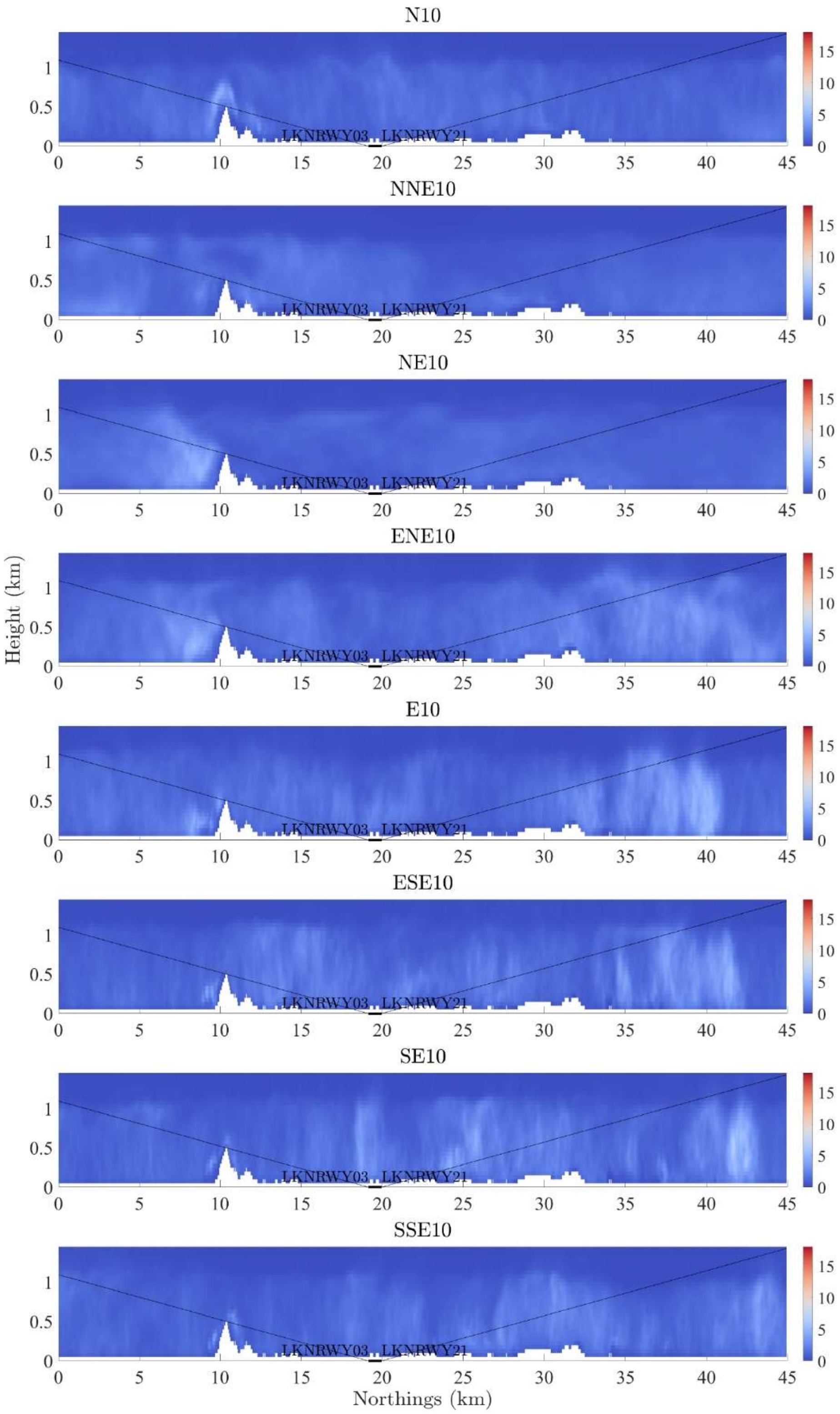


**Figure A5.** Vertical cross sections of the turbulence distribution ($m^2s^{-2}$) along the LKN runway for the simulations of set10.

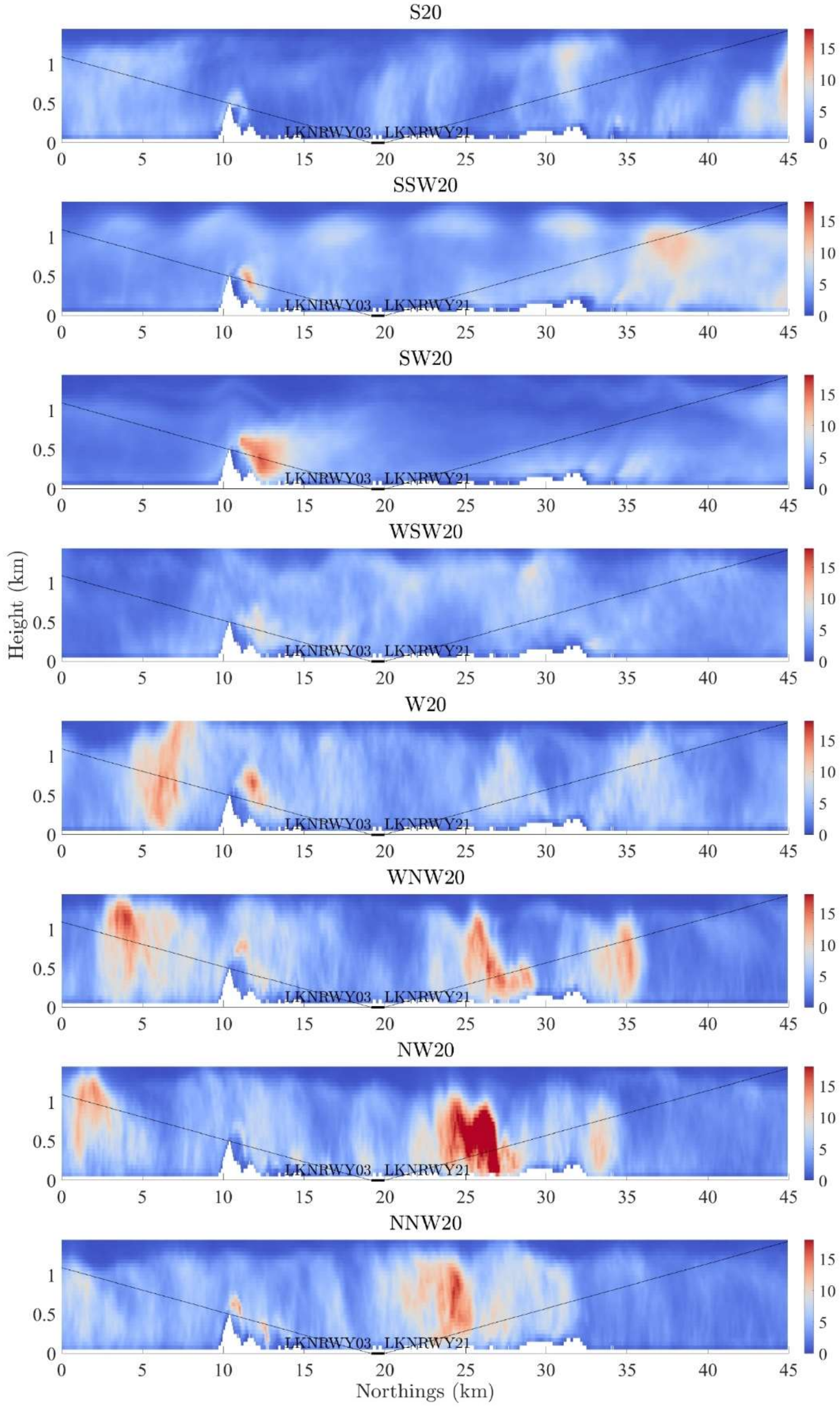


**Figure A6.** *Cont*.

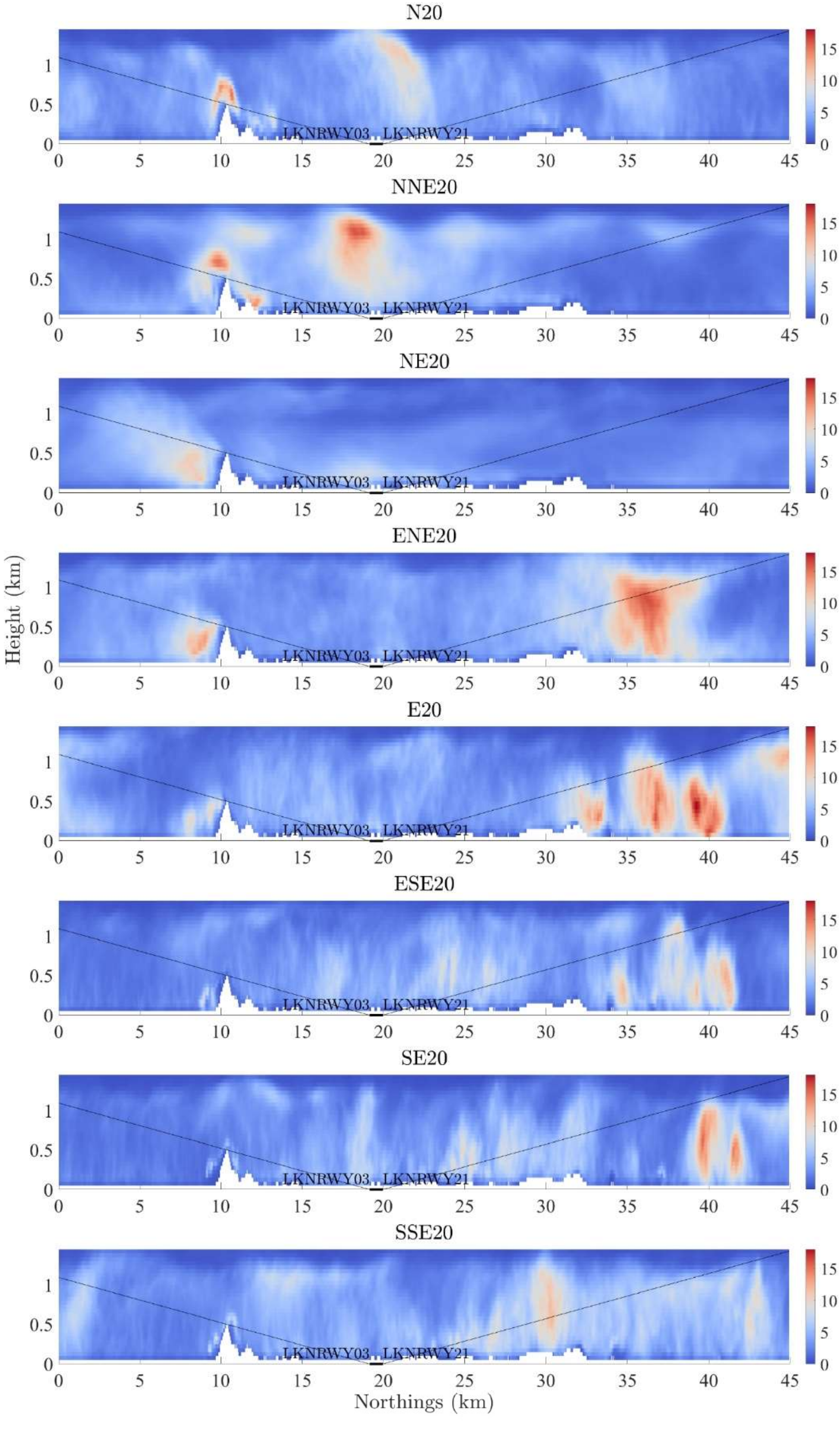


**Figure A6.** Vertical cross sections of the turbulence distribution ($m^2s^{-2}$) along the LKN runway for the simulations of set20.

## References


1. Sharman, R.; Lane, T. (Eds.) *Aviation Turbulence*; Springer International Publishing: Cham, Switzerland, 2016. [CrossRef]
2. Gultepe, I.; Sharman, R.; Williams, P.D.; Zhou, B.; Ellrod, G.; Minnis, P.; Trier, S.; Griffin, S.; Yum, S.S.; Gharabaghi, B.; et al. A Review of High Impact Weather for Aviation Meteorology. *Pure Appl. Geophys.* **2019**, *176*, 1869–1921. [CrossRef]
3. WMO. Aviation | Hazards | Turbulence and Wind Shear. Available online: https://community.wmo.int/activity-areas/aviation/hazards/turbulence (accessed on 1 March 2022).
4. Stull, R.B. *An Introduction to Boundary Layer Meteorology*; Springer: Dordrecht, The Netherlands, 1988. [CrossRef]
5. Sharman, R.D.; Trier, S.B.; Lane, T.P.; Doyle, J.D. Sources and dynamics of turbulence in the upper troposphere and lower stratosphere: A review. *Geophys. Res. Lett.* **2012**, *39*. [CrossRef]
6. Trier, S.B.; Sharman, R.D.; Lane, T.P. Influences of Moist Convection on a Cold-Season Outbreak of Clear-Air Turbulence (CAT). *Mon. Weather Rev.* **2012**, *140*, 2477–2496. [CrossRef]
7. Kim, J.H.; Chun, H.Y. Statistics and Possible Sources of Aviation Turbulence over South Korea. *J. Appl. Meteorol. Climatol.* **2011**, *50*, 311–324. [CrossRef]
8. Doyle, J.D.; Jiang, Q.; Smith, R.B.; Grubišić, V. Three-dimensional characteristics of stratospheric mountain waves during T-REX. *Mon. Weather Rev.* **2011**, *139*, 3–23. [CrossRef]
9. Lane, T.P.; Sharman, R.D.; Trier, S.B.; Fovell, R.G.; Williams, J.K. Recent Advances in the Understanding of Near-Cloud Turbulence. *Bull. Am. Meteorol. Soc.* **2012**, *93*, 499–515. [CrossRef]
10. Hon, K.K.; Chan, P.W. Alerting of hectometric turbulence features at Hong Kong International Airport using a short-range LIDAR. *Meteorol. Appl.* **2020**, *27*, 1–10. [CrossRef]
11. Smagorinsky, J. General circulation experiments with the primitive equations: I. The basic experiment. *Mon. Weather Rev.* **1963**, *91*, 99–164. [CrossRef]
12. van Heerwaarden, C.C.; Mellado, J.P. Growth and Decay of a Convective Boundary Layer over a Surface with a Constant Temperature. *J. Atmos. Sci.* **2016**, *73*, 2165–2177. [CrossRef]
13. Rai, R.K.; Berg, L.K.; Pekour, M.; Shaw, W.J.; Kosovic, B.; Mirocha, J.D.; Ennis, B.L. Spatiotemporal Variability of Turbulence Kinetic Energy Budgets in the Convective Boundary Layer over Both Simple and Complex Terrain. *J. Appl. Meteorol. Climatol.* **2017**, *56*, 3285–3302. [CrossRef]
14. Huang, J.; Bou-Zeid, E. Turbulence and Vertical Fluxes in the Stable Atmospheric Boundary Layer. Part I: A Large-Eddy Simulation Study. *J. Atmos. Sci.* **2013**, *70*, 1513–1527. [CrossRef]
15. Sullivan, P.P.; Weil, J.C.; Patton, E.G.; Jonker, H.J.J.; Mironov, D.V. Turbulent Winds and Temperature Fronts in Large-Eddy Simulations of the Stable Atmospheric Boundary Layer. *J. Atmos. Sci.* **2016**, *73*, 1815–1840. [CrossRef]
16. van der Linden, S.J.A.; Edwards, J.M.; van Heerwaarden, C.C.; Vignon, E.; Genthon, C.; Petenko, I.; Baas, P.; Jonker, H.J.J.; van de Wiel, B.J.H. Large-Eddy Simulations of the Steady Wintertime Antarctic Boundary Layer. *Bound. Layer Meteorol.* **2019**, *173*, 165–192. [CrossRef]
17. Bechmann, A.; Sørensen, N.N.; Berg, J.; Mann, J.; Réthoré, P.E. The Bolund Experiment, Part II: Blind Comparison of Microscale Flow Models. *Bound. Layer Meteorol.* **2011**, *141*, 245–271. [CrossRef]
18. Liu, Z.; Cao, S.; Liu, H.; Ishihara, T. Large-Eddy Simulations of the Flow Over an Isolated Three-Dimensional Hill. *Bound. Layer Meteorol.* **2019**, *170*, 415–441. [CrossRef]
19. Vollmer, L.; Steinfeld, G.; Heinemann, D.; Kühn, M. Estimating the wake deflection downstream of a wind turbine in different atmospheric stabilities: An LES study. *Wind Energy Sci.* **2016**, *1*, 129–141. [CrossRef]
20. Martínez-Tossas, L.A.; Churchfield, M.J.; Yilmaz, A.E.; Sarlak, H.; Johnson, P.L.; Sørensen, J.N.; Meyers, J.; Meneveau, C. Comparison of four large-eddy simulation research codes and effects of model coefficient and inflow turbulence in actuator-line-based wind turbine modeling. *J. Renew. Sustain. Energy* **2018**, *10*, 033301. [CrossRef]
21. Abkar, M.; Porté-Agel, F. Influence of atmospheric stability on wind-turbine wakes: A large-eddy simulation study. *Phys. Fluids* **2015**, *27*, 035104. [CrossRef]
22. Taylor, A.C.; Beare, R.J.; Thomson, D.J. Simulating Dispersion in the Evening-Transition Boundary Layer. *Bound. Layer Meteorol.* **2014**, *153*, 389–407. [CrossRef]
23. Resler, J.; Eben, K.; Geletič, J.; Krč, P.; Rosecký, M.; Sühring, M.; Belda, M.; Fuka, V.; Halenka, T.; Huszár, P.; et al. Validation of the PALM model system 6.0 in a real urban environment: a case study in Dejvice, Prague, the Czech Republic. *Geosci. Model Dev.* **2021**, *14*, 4797–4842. [CrossRef]
24. Knigge, C.; Raasch, S. Large-Eddy Simulation on the Influence of Buildings on Aircraft during Take Off and Landing. Available online: https://www.researchgate.net/publication/268648516_Large-eddy_simulation_on_the_influence_of_buildings_on_aircraft_during_take_off_and_landing (accessed on 18 April 2022).
25. Bergot, T.; Escobar, J.; Masson, V. Effect of small-scale surface heterogeneities and buildings on radiation fog: Large-eddy simulation study at Paris-Charles de Gaulle airport. *Q. J. R. Meteorol. Soc.* **2015**, *141*, 285–298. [CrossRef]
26. Chan, P.W.; Lai, K.K.; Li, Q.S. High-resolution (40 m) simulation of a severe case of low-level windshear at the Hong Kong International Airport—Comparison with observations and skills in windshear alerting. *Meteorol. Appl.* **2021**, *28*, 1–25. [CrossRef]
27. Liu, X.; Abà, A.; Capone, P.; Manfriani, L.; Fu, Y. Atmospheric Disturbance Modelling for a Piloted Flight Simulation Study of Airplane Safety Envelope over Complex Terrain. *Aerospace* **2022**, *9*, 103. [CrossRef]

28. WMO. *Aircraft Meteorological Data Relay (AMDAR) Reference Manual*; Technical Report 958; World Meteorological Organization (WMO): Geneva, Switzerland, 2003.
29. Sharman, R. Nature of Aviation Turbulence. In *Aviation Turbulence: Processes, Detection, Prediction*; Springer International Publishing: Cham, Switzerland, 2016; pp. 3–30. [CrossRef]
30. Rasheed, A.; Mushtaq, A. Numerical analysis of flight conditions at the Alta airport, Norway. *Aviation* **2014**, *18*, 109–119. [CrossRef]
31. Midtbø, K.H.; Bremnes, J.B.; Homleid, M.; Ødegaard, V. *Verification of Wind Forecasts for the Airports*; Technical Report 2; Norwegian meteorological Institute: Oslo, Norway, 2008.
32. Rasheed, A.; Sørli, K. CFD analysis of terrain induced turbulence at Kristiansand airport, Kjevik. *Aviation* **2013**, *17*. [CrossRef]
33. Øystein Ingebrigtsen. På Disse fire Stedene vil Avinor Måle Vind og Turbulens: -Vi Skal Sette ut Lasermålere i et Halvt år. Available online: https://www.lofotposten.no/flyplass/samferdsel/leknes/pa-disse-fire-stedene-vil-avinor-male-vind-og-turbulens-vi-skal-sette-ut-lasermalere-i-et-halvt-ar/s/5-29-379163 (accessed on 14 May 2018).
34. Website. Technical Documentation of PALM-Governing Equations. Available online: https://palm.muk.uni-hannover.de/trac/wiki/doc/tec/gov (accessed on 29 August 2019).
35. Wicker, L.J.; Skamarock, W.C. Time-Splitting Methods for Elastic Models Using Forward Time Schemes. *Mon. Weather Rev.* **2002**, *130*, 2088–2097. [CrossRef]
36. Williamson, J. Low-storage Runge-Kutta schemes. *J. Comput. Phys.* **1980**, *35*, 48–56. [CrossRef]
37. Deardorff, J.W. Cloud Top Entrainment Instability. *J. Atmos. Sci.* **1980**, *37*, 131–147. [CrossRef]
38. Moeng, C.H.; Wyngaard, J.C. Spectral Analysis of Large-Eddy Simulations of the Convective Boundary Layer. *J. Atmos. Sci.* **1988**, *45*, 3573–3587. [CrossRef]
39. Saiki, E.M.; Moeng, C.H.; Sullivan, P.P. Large-eddy simulation of the stably stratified planetary boundary layer. *Bound. Layer Meteorol.* **2000**, *95*, 1–30. [CrossRef]
40. Maronga, B.; Gryschka, M.; Heinze, R.; Hoffmann, F.; Kanani-Sühring, F.; Keck, M.; Ketelsen, K.; Letzel, M.O.; Sühring, M.; Raasch, S. The Parallelized Large-Eddy Simulation Model (PALM) version 4.0 for atmospheric and oceanic flows: Model formulation, recent developments, and future perspectives. *Geosci. Model Dev.* **2015**, *8*, 2515–2551. [CrossRef]
41. Maronga, B.; Banzhaf, S.; Burmeister, C.; Esch, T.; Forkel, R.; Fröhlich, D.; Fuka, V.; Gehrke, K.F.; Geletič, J.; Giersch, S.; et al. Overview of the PALM model system 6.0. *Geosci. Model Dev.* **2020**, *13*, 1335–1372. [CrossRef]
42. Kartverket-API og Data. Available online: https://www.kartverket.no/api-og-data (accessed on 10 January 2022).
43. Geonorge-Kartkalalogen. Available online: https://www.geonorge.no/ (accessed on 10 January 2022).
44. Kim, H.G.; Patel, V. Test of turbulence models for wind flow over terrain with separation and recirculation. *Bound. Layer Meteorol.* **2000**, *94*, 5–21. [CrossRef]
45. Agee, E.; Gluhovsky, A. LES Model Sensitivities to Domains, Grids, and Large-Eddy Timescales. *J. Atmos. Sci.* **1999**, *56*, 599–604. [CrossRef]
46. Wyngaard, J. Lectures on the planetary boundary layer. In *Mesoscale Meteorology—Theories, Observations and Models*; Springer: Berlin, Germany, 1983; pp. 603–650.
47. Lewis, M.S.; Robinson, P.A.; Hinton, D.A.; Bowles, R.L. *The Relationship of an Integral Wind Shear Hazard to Aircraft Performance Limitations*; NASA Technical Memorandum 109080; National Aeronautics and Space Administration, Langley Research Center, National Technical Information Service: Hampton, VA, USA, 1994.
48. Eidsvik, K.J.; Holstad, A.; Lie, I.; Utnes, T. A prediction system for local wind variations in mountainous terrain. *Bound. Layer Meteorol.* **2004**, *112*, 557–586. [CrossRef]
49. Clark, T.L.; Keller, T.; Coen, J.; Neilley, P.; Hsu, H.M.; Hall, W.D. Terrain-induced turbulence over Lantau Island: 7 June 1994 tropical storm Russ case study. *J. Atmos. Sci.* **1997**, *54*, 1795–1814. [CrossRef]
50. Ribbens, W. Aircraft Instruments, XVI. Instrument Landing System (ILS). In *Encyclopedia of Physical Science and Technology*, 3rd ed.; Meyers, R.A., Ed.; Academic Press: New York, NY, USA, 2003; pp. 337–364. [CrossRef]
51. Wurps, H.; Steinfeld, G.; Heinz, S. Grid-resolution requirements for large-eddy simulations of the atmospheric boundary layer. *Bound. Layer Meteorol.* **2020**, *175*, 179–201. [CrossRef]
52. Belcher, S.E.; Wood, N. Form and wave drag due to stably stratified turbulent flow over low ridges. *Q. J. R. Meteorol. Soc.* **1996**, *122*, 863–902. [CrossRef]
53. Hunt, J.C.R.; Leibovich, S.; Richards, K.J. Turbulent shear flows over low hills. *Q. J. R. Meteorol. Soc.* **1988**, *114*, 1435–1470. [CrossRef]
54. Chan, P.W. LIDAR-Based Turbulence Intensity for Aviation Applications. In *Aviation Turbulence*; Springer International Publishing: Cham, Switzerland, 2016; pp. 193–209. [CrossRef]
55. Potekaev, A.; Shamanaeva, L.; Kulagina, V. Spatiotemporal Dynamics of the Kinetic Energy in the Atmospheric Boundary Layer from Minisodar Measurements. *Atmosphere* **2021**, *12*, 421. [CrossRef]

# The LIKE project in brief

The project LIKE Lidar Knowledge Europe H2020-MSCA-ITN-2019, Grant no. 858358 is funded by the European Union and project partners.

The project partners are DTU Wind Energy (DK, co-ordinator), University of Oldenburg (DE), University in Bergen (NO), University Stuttgart (DE), PoliTechnico Milano (IT), University Porto (PT), University in Stavanger (NO), Flensburg University of Applied Sciences (DE), Fraunhofer IWES (DE) and UL (DE).

The project period is from 1st October 2019 to 30th September 2023 (4 years).

LIKE fosters training and education of young researchers on emerging laser-based wind measurement technologies and their translation into industrial applications.

Doppler Lidars (light detection and ranging) that measure the wind in the atmosphere remotely have reduced in price and increased in reliability over the last decade mainly done by European universities and companies serving the growing wind energy industry. This opens the possibility for new applications in many areas.

LIKE improves, tests and refines the technology thus expanding these areas of application. LIKE promotes wind energy applications such as wind resource mapping using scanning lidars and control of single wind turbines or entire wind farms in order to increase energy production and reduce mechanical loads.

LIKE maps unusual atmospheric flow patterns over airports in real-time and thus improves the safety of landing aircrafts. LIKE explores wind and turbulence under extreme conditions at the sites of future European bridges paving the road for optimal bridge design. LIKE trains 15 ESRs to an outstanding level at European academic institutions and industrial companies, thus forming strong interdisciplinary relations between industry and technical sciences.

These relations are implemented through employment of the ESRs at academia as well as industry, and through inter-sectoral secondments.

Project web-site is http://www.msca-like.dk/